RADBOUD UNIVERSITY NIJMEGEN

MASTER THESIS

Comparisons of computational tools for the muon anomalous magnetic moment within the pMSSM

Author:
Jeremy de Wit
s4349504
Jeremy.dewit@gmail.com

Supervisor:
Prof. dr. W.J.P. Beenakker
M.C. van Beekveld
M.T. Schutten

Second corrector:
dr. C.W.J.P. Timmermans

Theoretical High Energy Physics

August 25, 2020

Contents

Introduction

The Standard Model (SM) is one of the best tested theories in physics. It categorizes all elementary particles, their properties and their interactions via three of the four fundamental forces: the electromagnetic, weak and strong force. In this thesis we will examine a property called the magnetic moment for one of these elementary particles: the muon.

Any elementary particle with intrinsic properties of spin and charge, will produce a magnetic moment. This includes the quarks and the charged leptons. The muon is part of the lepton family. For the first two leptons, the electron and the muon, the magnetic moment has been calculated theoretically up to a very high precision. Experiments have been and are being set up to measure the magnetic moment of these leptons to an equally high precision.

When one calculates the magnetic moment of a lepton, one starts with the first-order calculation of this effect. The magnetic moment can be decomposed in a numerical factor multiplied by the Bohr magneton μ_B divided by the reduced Planck constant $\hbar$. This numerical factor is 2 at lowest order, but if we include quantum corrections it will deviate from this value. This deviation is called the anomalous magnetic moment a_l, where l indicates the lepton considered.

Any experiment measuring the anomalous magnetic moment would automatically take into account all higher-order corrections. A theoretical calculation can only account up to a certain number of higher-orders. As the theoretical and experimental value do not agree within the bounds of their respective uncertainties, there is a possibility for a measurement of new physics affecting the anomalous magnetic moment of the leptons. The discrepancy between the theoretical and experimental value has been steadily increasing over the last decade due to a higher precision in experiments and theoretical calculations.

The experimental and theoretical values of the anomalous magnetic moment for the lightest two leptons are [1][2][3]:

$$\begin{aligned} a_e^{\text{exp}} &= 11596521807.3 \cdot 10^{-13}, \\ a_e^{\text{SM}} &= 11596521817.8 \cdot 10^{-13}, \end{aligned}$$

$$\begin{aligned} a_\mu^{\text{exp}} &= 116592091 \cdot 10^{-11}, \\ a_\mu^{\text{SM}} &= 116591830 \cdot 10^{-11}. \end{aligned}$$

We will show and discuss the uncertainties on the relevant values in chapter 1.8. The third lepton, the tau lepton, has been omitted here as the experimental and theoretical value of its magnetic moment have not been precisely determined yet. This is because the tau lepton is too short-lived. For current values of the anomalous magnetic moment of the tau lepton, see [4].

As can be seen above, the experimental and theoretical values to not agree with each other. The discrepancy for the muon is 3.3σ, which is more significant than for the electron. The muon discrepancy is given by $\Delta a_\mu = 2.61 \cdot 10^{-9}$. This is the first reason why we choose to look at the anomalous magnetic moment of the muon. Secondly, it is more susceptible to new physics effects. This is because the contributions to a_l scale with the mass of the lepton:

$$\frac{\delta a_l}{a_l} \propto \frac{m_l^2}{M^2}, \qquad M \gg m_l. \tag{I.1}$$

Here, m_l is the mass of the lepton. With this we can estimate how much a_l is influenced by new physics that starts to take effect at a mass scale M. For example, we can estimate the effect of the weak interactions at $M = m_W$ compared to a calculation including only QED. We see that a heavier lepton is influenced more strongly due to the factor m_l.

To account for the discrepancy, we have to alter the SM. One of the possible extensions is called the minimal supersymmetric standard model (MSSM). In the MSSM, a (broken) symmetry between fermions and bosons is added to the SM. This would (more than) double the number of existing particles.

The MSSM adds over a hundred new free parameters. This number can be reduced with additional assumptions. A model that implements a number of these assumptions is the phenomenological MSSM (pMSSM), which we will look into more closely. It reduces the number of free parameters to 19. Using specific values for these parameters, one can determine the particle spectrum of the theory. This is typically done by using a spectrum generator, e.g. SPheno. One can also calculate observables based on the particle spectrum and parameter values, for which there are a multitude of programs available. However, for the same input, the results from these programs can differ.

In this thesis we will examine the differences between the output of the programs SuperISO and MicrOMEGAs for the pMSSM contribution to the anomalous magnetic moment of the muon. We focus on these two programs, as they are widely used in the SUSY theory community. When providing these programs the same input, their output can be significantly different for δa_μ. We will explain why this happens and which program should be prioritised for δa_μ calculations.

In chapter 1 we will lay the theoretical groundwork required for calculations of the anomalous magnetic moment within the SM. It will feature the types of Feynman diagrams that are relevant for the anomalous magnetic moment and techniques on how to evaluate their relevant parts. In chapter 2 we will give an overview of the supersymmetric extension of the SM that we will consider. In chapter 3 we will introduce the additional Feynman diagrams in the pMSSM. We will use these to show which pMSSM parameters are significant for δa_μ. Finally, in chapter 4 we will introduce the program SPheno, MicrOMEGAs and SuperISO. The latter two will be used for calculating δa_μ. We will show the difference in output between MicrOMEGAs and SuperISO and explain why the difference exists.

Conventions

We will use the mostly negative signature for the metric:

$$\eta_{\mu\nu} = \text{diag}(+1, -1, -1, -1).$$

When repeated indices occur, we will use the Einstein summation convention given by:

$$x^\mu x_\mu = (x^0)^2 - (x^1)^2 - (x^2)^2 - (x^3)^2.$$

We will use Feynman slash notation:

$$\not{p} = \gamma^\mu p_\mu,$$

where the γ-matrices are defined as:

$$\gamma^0 = \begin{pmatrix} \mathbb{1}_2 & 0 \\ 0 & -\mathbb{1}_2 \end{pmatrix}, \qquad \gamma^i = \begin{pmatrix} 0 & \sigma^i \\ -\sigma^i & 0 \end{pmatrix}, \qquad \gamma^5 = \begin{pmatrix} 0 & \mathbb{1}_2 \\ \mathbb{1}_2 & 0 \end{pmatrix},$$

where i can be 1, 2 or 3 and $\mathbb{1}_2$ is the 2-dimensional identity matrix. The product of γ-matrices is given by $\gamma^5 = i\gamma^0\gamma^1\gamma^2\gamma^3$. The pauli spin matrices, σ^i, are given by:

$$\sigma^1 = \begin{pmatrix} 0 & 1 \\ 1 & 0 \end{pmatrix}, \qquad \sigma^2 = \begin{pmatrix} 0 & -i \\ i & 0 \end{pmatrix}, \qquad \sigma^3 = \begin{pmatrix} 1 & 0 \\ 0 & -1 \end{pmatrix}.$$

A useful combination of the γ-matrices is:

$$\sigma^{\mu\nu} = \frac{i}{2}\Big(\gamma^\mu\gamma^\nu - \gamma^\nu\gamma^\mu\Big).$$

The partial derivative is defined as:

$$\partial_\mu = \frac{\partial}{\partial x^\mu}.$$

We will denote the difference between experimental value and the SM theoretical value of the anomalous magnetic moment as Δa_μ. When we calculate a contribution to a_μ from a specific diagram or process we denote this contribution with δa_μ.

Before chapter 1.5, standard SI units will be used. Starting in chapter 1.5 and onward, natural units ($\hbar = c = 1$) will be used.

We will make use of the fractional charge Q at certain points in the thesis:

$$q = Qe,$$

with q being charge and e the elementary charge. Q is then just a number, i.e. -1 for the electron.

The uncertainties determined for theoretical and experimental results will be denoted within parenthesis behind the result itself. The value inside parenthesis is to be taken as the uncertainty on the last digits of the result. The amount of digits inside

the parenthesis give the amount of last digits of the result that are unsure. Example:

$$x = 123456(78) \implies 123378 < x < 123534,$$
$$y = 7654.3(2.1) \implies 7652.2 < y < 7656.4.$$

Certain results will include multiple uncertainties coming from different sources, they will be represented by multiple parenthesised numbers following the result.

Chapter 1

The anomalous magnetic moment within the SM

1.1 Classical magnetic moment

To get an understanding of the anomalous magnetic moment within the SM, we first need to look at the classical concept of the magnetic moment, rooted in electrodynamics.

The magnetic moment is an intrinsic property of an object or particle, and defines how it reacts when exposed to an externally applied magnetic field. It can be thought of as a magnetic dipole that, when disaligned inside a magnetic field, will start to precess. This precession is due to the torque created by the force of the external magnetic field on the current created by the object or particle. The magnetic dipole moment $\vec{\mu}$ is defined as

$$\vec{\mu} = \frac{1}{2}\int_V \vec{r} \times \vec{j}\, \mathrm{d}V,$$

where $\vec{r}$ is the position vector with respect to the center of mass of the volume V that we integrate over and $\vec{j}$ is the current density inside this volume [5].

If we consider a simple charged object rotating in a circle around some centre point at a relative distance $\vec{r}$, the above expression becomes the product of the displaced charge (current) and the area it encloses. It was thought historically that this is how an electron revolves around a proton. This is shown inside an external magnetic field in figure 1.1, where the torque created by this external field is illustrated as well. The magnetic moment for such a system is given by

$$\vec{\mu} = \frac{1}{2}\int \vec{r} \times \vec{j}\, \mathrm{d}l = \frac{1}{2}\int \vec{r} \times \frac{qv}{2\pi r}\, \mathrm{d}\vec{l} = \frac{qv}{2\pi r}\pi r^2 \hat{n} = -\frac{e}{2m_e}\vec{L} \equiv -\frac{ge}{2m_e}\vec{L}. \tag{1.1}$$

Here, q is the charge of the object ($-e$ in the case of the electron, used in the last equality), v its velocity and $\vec{L}$ the orbital angular momentum of the object. The mass in the equation belongs to the particle in the current loop, m_e in the above case. Note that the magnetic moment and the angular momentum are directly related. The quantity g has been added artificially in the last equivalence. Classically, $g = 1$. It is often referred to as the dimensionless magnetic moment or the g-factor. It is defined as

$$g = \gamma_m \frac{\hbar}{\mu_B},$$

where $\gamma_m = |\vec{\mu}|/|\vec{L}| = \mu/L$ is the gyromagnetic ratio, which measures the ratio of the magnetic moment and angular momentum. For elementary particles, we can

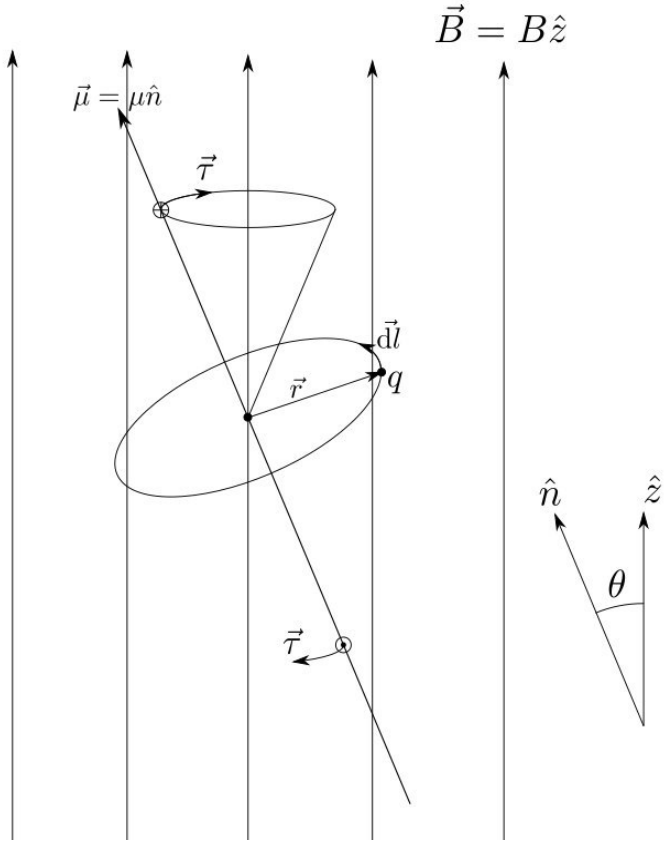

FIGURE 1.1: The definition of the magnetic moment for a simple charge loop with the illustration of the created torque by an external magnetic field. The charge of the particle in the figure is taken to be positive.

express this ratio in terms of the Bohr magneton:

$$\gamma_m = \frac{\mu}{L} = -g\frac{e}{2m} = -g\frac{\mu_B}{\hbar}, \text{ with } \mu_B = \frac{e\hbar}{2m}.$$

The quantum mechanical concept of spin will contribute to the angular momentum of an elementary particle, thus increasing its g-factor. At first glance, the g-factor will become 2, but radiative corrections will increase its value slightly. These aspects will be discussed in chapter 1.5.

To identify which (quantum mechanical) terms affect the magnetic moment we will need to look at the potential energy caused by a magnetic dipole. Using the circular loop example in figure 1.1 will aid our discussion. The torque $\vec{\tau} = \vec{\mu} \times \vec{B}$ that the circular current experiences when inside an external magnetic field, causes work to be done and, in turn, causes a change in the potential energy. If we assume the angle between the magnetic field and the magnetic moment to be θ, we can derive the potential energy by integrating with respect to an arbitrary reference point:

$$U = \int \vec{\tau} \cdot d\vec{\theta} = \int \mu B \sin\theta' d\theta' = -\vec{\mu} \cdot \vec{B}. \tag{1.2}$$

1.2 Magnetic moment in quantum field theory

The concept of spin modifies the magnetic moment and the dimensionless gyromagnetic ratio, even when the orbital angular moment is zero. An example of this would be a 'free' electron.

A system of free spin-$\frac{1}{2}$ particles of mass m, represented by the Dirac field ψ, and antiparticles of mass m represented by the Dirac field $\bar{\psi}$, is described by the Dirac Lagrangian

$$\mathscr{L} = i\hbar c\bar{\psi}(x)\partial\!\!\!/\psi(x) - mc^2\bar{\psi}(x)\psi(x).$$

The Lagrangian consists of a kinetic term and a mass term for the particle fields. No interaction term is present. Solving the Euler-Lagrange equations for this Lagrangian leads to the Dirac equation:

$$(i\hbar\partial\!\!\!/ - mc)\psi(x) = 0. \tag{1.3}$$

The Lagrangian is invariant under a global $U(1)$ transformation. However, when invoking the gauge principle by imposing invariance under local $U(1)$ transformations:

$$\psi(x) \to e^{-ie\alpha(x)/\hbar}\psi(x),$$
$$\bar{\psi}(x) \to e^{ie\alpha(x)/\hbar}\bar{\psi}(x),$$

this is no longer true. The transformed Lagrangian will have an extra term violating invariance. To prevent this term, the derivative can be modified to produce a counter term. To this end, a new gauge field A_ν must be introduced which transforms as:

$$\partial_\nu \to D_\nu = \partial_\nu - \frac{ie}{\hbar}A_\nu(x),$$

$$A_\nu \to A_\nu - \partial_\nu\alpha(x).$$

The $\psi(x)$ fields still describe (charged) spin-$\frac{1}{2}$ leptons. The new gauge field A_ν can be identified as the photon field. A new term will now be present in the Lagrangian, describing the interaction between the leptons and the photons. The photon field also has its own kinetic and mass term. However, the mass term needs to be zero in order to preserve $U(1)$ local gauge invariance. The Quantum Electrodynamics (QED) Lagrangian is then found [6]:

$$\mathscr{L}_{QED} = i\hbar c\bar{\psi}(x)\partial\!\!\!/\psi(x) - mc^2\bar{\psi}(x)\psi(x) - \frac{1}{4}F_{\nu\rho}F^{\nu\rho} + ec\bar{\psi}(x)\gamma^\nu A_\nu(x)\psi(x), \tag{1.4}$$

where $F_{\nu\rho} = \partial_\nu A_\rho - \partial_\rho A_\nu$ is the electromagnetic field tensor, describing the kinetic term of the photon field.

To find the magnetic moment of the leptons with charge q, one needs to evaluate the Dirac equation in an external magnetic field. This is because the magnetic moment of a particle or system can only be measured or tested by subjecting it to a magnetic field. We thus need to modify equation 1.3 to include the (covariant) derivative for an external magnetic field. The result is:

$$(i\hbar\partial\!\!\!/ + eA\!\!\!/_\nu - mc)\psi(x) = 0.$$

Trying to solve this relativistically is complex. One usually tries a unitary transformation to remove the γ operators from the Dirac equation, but this is not possible in the relativistic case up to all orders. Fortunately, the non-relativistic limit is already insightful. In this limit, we only consider terms up to order $\frac{p}{mc}$. The above differential equation can then be rewritten into the Pauli equation with a specific unitary transformation. We omit the derivation of the general transformation here, see [7] and [8] for more details. After the transformations, the four-component Dirac fields $\psi(x)$ are split into two-component Pauli spinors. We only consider the dominant (at non-relativistic energies) component: φ. The Pauli equation is then found:

$$i\hbar\frac{\partial\hat{\varphi}}{\partial t} = \Big(\frac{1}{2m}\big(-i\hbar\vec{\nabla} + e\vec{A}\big)^2 + e\Phi + \frac{e\hbar}{2m}\vec{\sigma}\cdot\vec{B}\Big)\hat{\varphi}. \tag{1.5}$$

In equation 1.5, the electromagnetic field is split up in components Φ and $\vec{A}$ according to $A^\nu = (\Phi/c, \vec{A})$. The Pauli matrices are denoted by $\vec{\sigma}$. The Pauli equation closely resembles the Schrödinger equation except for the extra term involving the magnetic field. Using equation 1.2, this term is interpreted as the potential energy of the magnetic dipole moment with:

$$\vec{\mu}_s = -\frac{e\hbar}{2m}\vec{\sigma} = -\frac{e}{m}\vec{S}, \tag{1.6}$$

where $\vec{S} = \hbar\frac{\vec{\sigma}}{2}$ is the angular momentum due to spin. Defining $g = g_l$ for the classical result in equation 1.1 and adding it to 1.6, we find

$$\vec{\mu}_{tot} = \vec{\mu_l} + \vec{\mu_s} = -\frac{e}{2m}\big(g_l\vec{L} + g_s\vec{S}\big) = -\frac{\mu_B}{\hbar}\big(g_l\vec{L} + g_s\vec{S}\big).$$

We have $g_l = 1$ and now find $g_s = 2$ as done by Dirac in 1928 [9].

Radiative corrections also add to g_s, causing a deviation from $g_s = 2$. We can quantify this deviation in a renormalisable theory. This quantity is called the anomalous magnetic moment and is given by

$$a_\mu = \frac{g-2}{2}. \tag{1.7}$$

Here, the label for g has been removed as is convention, but it refers to g_s. Furthermore, μ denotes the muon, but this quantity can be determined for any charged particle or composite particle.

1.3 Current experiment

The claim that $a_\mu \neq 0$ due to quantum fluctuations has to be experimentally verified. The most precise experimental value has been established by the E821 experiment at Brookhaven National Laboratory (BNL) in 2001 [2]:

$$a_\mu^{\text{exp}} = 116592091(54)(33)\cdot 10^{-11}, \tag{1.8}$$

where the first (second) uncertainty indicates the statistical (systematic) uncertainty. The anomalous magnetic moment is a parity (P) and charge conjugation (C) conserving quantity, as such the experimental value is determined by taking the average of the muon and anti-muon measurements.

The basic principle of the E821 BNL experiment is to measure the frequency of the precession of the magnetic moment of the muon within a constant external magnetic field. This precession is referred to as Larmor precession. Its corresponding Larmor frequency is classically given by the product of the gyromagnetic ratio with the magnetic field. A relativistic correction has to be applied to get to the full spin precession ω_s, see [10]:

$$\vec{\omega}_s = \gamma_m \vec{B} + (1-\gamma)\frac{e\vec{B}}{\gamma m} = \frac{ge\vec{B}}{2m} + (1-\gamma)\frac{e\vec{B}}{\gamma m},$$

where $\gamma = \frac{1}{\sqrt{1-\beta^2}}$ is the Lorentz factor.
The frequency we are interested in is exactly the difference in frequency between the spin precession (ω_s) of the muon, and its (relativistic) cyclotron frequency (ω_c). The cyclotron frequency is given by [11]:

$$\vec{\omega}_c = \frac{e\vec{B}}{\gamma m}.$$

By measuring the spin and cyclotron frequency of muons moving in a large ring, we can thus determine the anomalous magnetic moment. The difference between these frequencies is defined as $\vec{\omega}_a$ and is given by:

$$\vec{\omega}_a = \vec{\omega}_s - \vec{\omega}_c = \frac{g-2}{2}\frac{e\vec{B}}{m}.$$

We see that if $g = 2$, $\vec{\omega}_a$ will vanish. The fact that it doesn't can be measured due to the spin frequency being disaligned with itself after each rotation in a circular ring. This is schematically depicted in figure 1.2.

A circular ring that measures $\vec{\omega}_a$ is the muon storage ring at the E821 experiment. For this experiment, the disalignment is roughly 12 degrees per rotation. To measure this, muons are injected into an external constant magnetic field at relativistic velocities. However, this requires electric fields to focus the muons. These fields alter the expression for $\vec{\omega}_a$, leading to the Thomas-Bargmann-Michel-Telegdi (BMT) equation [12]:

$$\vec{\omega}_a = \frac{e}{m_\mu}\Big(a_\mu \vec{B} - \Big[a_\mu - \frac{1}{\gamma^2-1}\Big]\frac{\vec{v}\times\vec{E}}{c^2}\Big),$$

This equation is split into a term caused by the magnetic field and a term caused by the (focusing) electric fields. The magnetic field term scales linearly with the anomalous magnetic moment. This means that a_μ could be determined directly, in absence of the electric field. However, as these fields are necessary to focus the muons, the experiment instead tries to minimise the contribution of this term. This is done by tuning the velocity of the muons such that the term in brackets becomes zero:

$$\gamma = \sqrt{1+\frac{1}{a_\mu}} \approx 29.3 \implies \Big[a_\mu - \frac{1}{\gamma^2-1}\Big] \approx 0.$$

This cannot be done exactly, as the value of a_μ is the quantity we wish to extract from this experiment. However, the contribution from the electric field can be approximated to vanish when tuning the velocity of the muons correctly. Fortunately, at this velocity, the muon is highly relativistic, increasing its lifetime just long enough for it to be measurable. This is why the muon is most interesting for measurements of the anomalous magnetic moment; it is the heaviest charged lepton which still

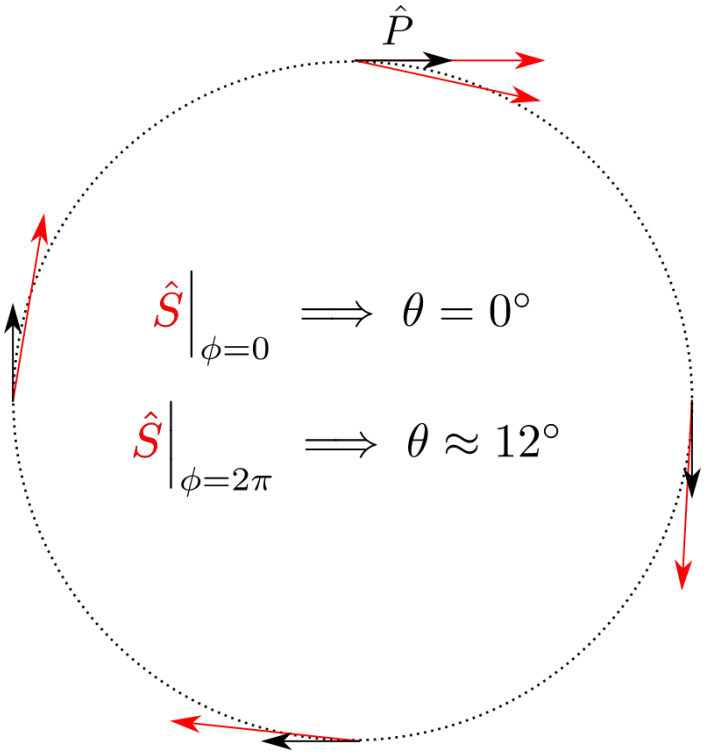

FIGURE 1.2: Schematic depiction of muons traveling in a circular ring. Muon injection takes place at the top of the circular ring. The momentum vector of the muons is given in black. The spin vector is given in red. After one full rotation at the BNL experiment, the spin vector is disaligned with the momentum vector by roughly $12°$.

lives long enough to be measured. The tau lepton decays seven orders of magnitude faster than the muon and as such is not suitable for this experiment.

The theoretically determined anomalous magnetic moment of the muon is given by:

$$a_\mu^{\mathrm{SM}} = 116591830(1)(40)(26) \cdot 10^{-11}. \tag{1.9}$$

We will see how this value and the uncertainties are determined in chapter 1.7 and 1.8. The discrepancy between the theoretical and experimental determination of a_μ is 3.3σ and has been one of the longest standing deviations between theory and experiment within the SM.

The latest experiment is set up at Fermilab and uses the same muon storage ring from BNL, performing the same experiment, but with an improved injection method and a longer run time [13]. It is expected to publish its first results in the summer of 2020. This new experiment should decrease the statistical uncertainty of the BNL experiment, which is the largest uncertainty as seen in equation 1.8. The result is expected to yield a four times smaller uncertainty. If the measured value does not change in this new experiment, the discrepancy between theory and experiment will increase to roughly 7σ. Since a discrepancy of at least 5σ is considered significant for the discovery of new physics, we will look into possible BSM explanations.

1.4 Brief summary of the SM

The SM is the most accurate and precisely tested theory in physics. It is a quantum field theory characterised by the following gauge symmetries:

$$SU(3)_C \otimes SU(2)_L \otimes U(1)_Y.$$

Each of these gauge symmetries corresponds to a fundamental force. The hypercharge force is governed by the $U(1)_Y$ gauge symmetry, where Y denotes the hypercharge. The $SU(3)_C$ gauge group represents the strong force, with C denoting the colour charge. The theory associated to it is called Quantum Chromodynamics (QCD). Lastly, $SU(2)_L$ is the gauge group belonging to the weak force. Here, L denotes the fact that the weak force only couples to left-handed particles. These are particles with a negative chirality. For massless particles, this corresponds to a negative helicity, i.e. particles for which the spin vector projected onto the momentum vector yield a negative result. The electromagnetic force is contained in this setup, hidden in the $U(1)_Y \otimes SU(2)_L$, see below.

The SM consists of two types of elementary particles; bosons and fermions. The bosons are the force carriers, which cause the specific interactions decribed above. They always have an integer spin. A special type of boson is the Higgs boson. It is responsible for giving mass to most SM particles. The fermions are the matter particles, and will have spin $\frac{1}{2}$. The quarks and leptons make up the fermions and are grouped into families and split into left-handed particle doublets and right-handed particles due to the bias towards left-handed particles by the weak force.

The three quark families each consist of an up-type and a down-type quark. The first family contains the up quark (u) and the down quark (d). The second family consists of the charm (c) and strange (s) quarks and the third family has the top (t) and bottom (b) quarks. The three lepton families are the electron (e), muon (μ) and tau (τ) with their corresponding neutrinos (ν). The particle content of the SM is summarised in table 1.1.

The electromagnetic and weak force are often combined into the electroweak (EW) force. This comes from combining $SU(2)_L \otimes U(1)_Y$. The EW gauge fields are given by the massless fields W^1, W^2, W^3 and B^0. Due to the Higgs mechanism, the $SU(2)_L \otimes U(1)_Y$ symmetry is broken, making the gauge fields combine into mass eigenstates. The W^1 and W^2 gauge fields combine into the W^+ and W^- boson. The W^3 and B^0 gauge fields combine into the Z boson and the photon (γ). The original gauge fields were massless, but the $W^\pm$ and Z boson gain a mass due to the symmetry breaking, whereas the photon remains massless.

The relationship between charge Q, weak isospin I_3 and hypercharge Y_W expresses that the electromagnetic force is hidden in $U(1)_Y \otimes SU(2)_L$:

$$Q = I_3 + \frac{1}{2} Y_W.$$

Anomalous magnetic moment
The anomalous magnetic moment is caused by interactions between the muon and all of the other SM particles. We will split up the contributions to the anomalous magnetic moment in a similar way as the gauge groups of the SM are divided. Any

SM particles	spin 0	spin $\frac{1}{2}$	spin 1	Q	I_3	Y_W
quarks (3 families)		$(u_L \quad d_L)$ u_R^C d_R^C		$(\frac{2}{3} \quad -\frac{1}{3})$ $-\frac{2}{3}$ $\frac{1}{3}$	$(\frac{1}{2} \quad -\frac{1}{2})$ 0 0	$(\frac{1}{3} \quad \frac{1}{3})$ $-\frac{4}{3}$ $\frac{2}{3}$
leptons (3 families)		$(\nu_L \quad e_L)$ e_R^C		$(0 \quad -1)$ 1	$(\frac{1}{2} \quad -\frac{1}{2})$ 0	$(-1 \quad -1)$ 2
Higgs	H			0	$-\frac{1}{2}$	1
gluon			g	0	0	0
W			$W^{\pm}$	± 1	± 1	0
Z			Z^0	0	0	0
photon			γ	0	0	0

TABLE 1.1: All particles present in the Standard Model with their corresponding spin, charge Q in units of e, weak isospin I_3 and hypercharge Y_W.

interaction governed by the strong force will be classified as a QCD contribution. Any interaction governed by the weak force, without a strong force being present, will be classified as an EW contribution. The interactions where only the electromagnetic force plays a part will be classified as Quantum Electrodynamics (QED) contributions.

1.5 QED contributions

As mentioned in the conventions, we will now adopt natural units:

$$\hbar = c = 1.$$

In QFT we typically calculate probability amplitudes and densities, and related to that matrix elements. By applying perturbation theory in the interaction strengths we find a diagrammatic representation called Feynman diagrams from which we extract quantities of interest. Only a part of the matrix element is relevant for Δa_μ. We will now derive the relevant part.

The deviations from $g = 2$ are caused by higher order effects in the vertex between a muon interacting with a photon, as described by the Lagrangian in equation 1.4. By using the Feynman rules in the Feynman-'t Hooft gauge as can be found in [14], we can compute the matrix element of the diagram in figure 1.3a. Note that the direction of time is upwards in these diagrams. At tree level, the matrix element is given by:

$$i\mathcal{M} = ie\bar{u}(p_2)\gamma^\nu u(p_1)\epsilon_\nu(q).$$

We will omit the polarisation vector $\epsilon_\nu(q)$, as this is not relevant for Δa_μ. The corresponding matrix element then has an open Lorentz index:

$$i\mathcal{M} = i\mathcal{M}^\nu \cdot \epsilon_\nu.$$

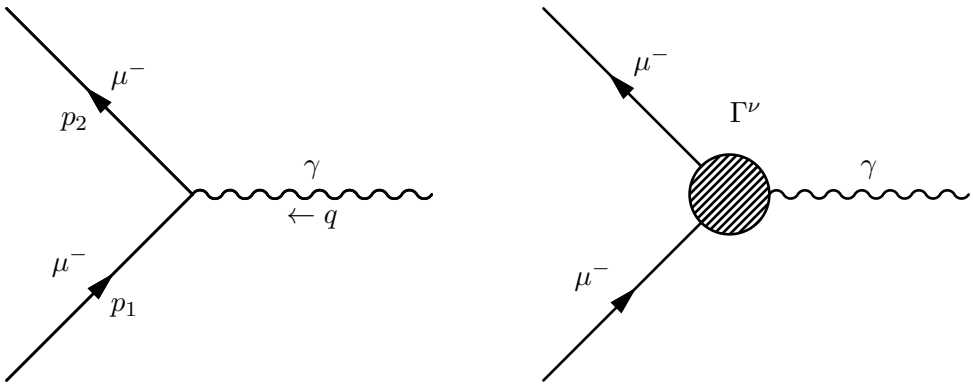

(A) The lowest order contribution to Δa_μ. (B) The diagram incorporating all loops.

FIGURE 1.3: The Feynman diagrams showing the lowest order contribution and the contribution up to all orders. The p_1, p_2 and q denote the momenta of the relevant particles.

We will continue to work with the $i\mathcal{M}^\nu$ matrix element from here on.

The matrix valued object between the spinors $\bar{u}(p_2)$ (outgoing muon) and $u(p_1)$ (incoming muon) is the cause of the open Lorentz index of the matrix element. It has to be there at any loop order. As such, the matrix element of the generic loop diagram of figure 1.3b can be postulated by introducing a generic function Γ^ν:

$$i\mathcal{M}^\nu = ie\bar{u}(p_2)\Gamma^\nu u(p_1). \tag{1.10}$$

As $\bar{u}(p_2)\gamma^\nu u(p_1)$ transforms as a vector, so must $\bar{u}(p_2)\Gamma^\nu u(p_1)$. Thus, it must be a linear combination of the vectors present in the diagram. We define the momentum of the incoming muon as p_1^ν, the momentum of the outgoing muon as p_2^ν and the momentum of the photon as q^ν. Analogous to Peskin and Schroeder [15], we then use these momenta and γ^ν to construct the possible contributions Γ^ν can have. In contrast to Peskin and Schroeder, we also include the parity violating terms caused by γ^5.

It is conventional to use the sum and difference of the incoming momenta as variables: $P^\nu = p_1^\nu + p_2^\nu$ and $q^\nu = p_2^\nu - p_1^\nu$. This results in 6 independent contributions:

$$\Gamma^\nu = \gamma^\nu A_1 + \frac{P^\nu}{2m}A_2 + \frac{q^\nu}{2m}A_3 + \gamma^\nu\gamma^5 A_4 + \frac{q^\nu}{2m}\gamma^5 A_5 + i\frac{P^\nu}{2m}\gamma^5 A_6. \tag{1.11}$$

This is called the covariant decomposition. It turns out $A_3 = 0$ and $A_5 = -4m^2q^{-2}A_4$ due to current conservation, see [16]. This leaves us with only four independent amplitudes which could possibly contribute. With help of the Gordon identities:

$$\begin{aligned}\bar{u}(p_2)\gamma^\nu u(p_1) &= \bar{u}(p_2)\frac{P^\nu}{2m}u(p_1) + \bar{u}(p_2)i\frac{\sigma^{\nu\rho}q_\rho}{2m}u(p_1),\\ \bar{u}(p_2)i\frac{P^\nu}{2m}\gamma^5 u(p_1) &= \bar{u}(p_2)\frac{\sigma^{\nu\rho}}{2m}q_\rho\gamma^5 u(p_1),\end{aligned} \tag{1.12}$$

some terms can be rearranged, leading to a generic expression for Γ^ν:

$$\Gamma^\nu = \gamma^\nu(A_1 + A_2) - i\frac{\sigma^{\nu\rho}q_\rho}{2m}A_2 + \left(\gamma^\nu - \frac{2mq^\nu}{q^2}\right)\gamma^5 A_4 + \frac{\sigma^{\nu\rho}q_\rho}{2m}\gamma^5 A_6.$$

Now we define form factors, which are functions of only the exchanged momentum q, that tell us something about the properties of the interaction between particles:

$$\begin{aligned} F_E &= A_1 + A_2, \\ F_M &= -A_2, \\ F_D &= A_6, \\ F_A &= A_4. \end{aligned}$$

We can rewrite Γ^ν in terms of the form factors:

$$\implies \Gamma^\nu = \gamma^\nu F_E + i\frac{\sigma^{\nu\rho}q_\rho}{2m}F_M + \left(\gamma^\nu - \frac{2mq^\nu}{q^2}\right)\gamma^5 F_A + \frac{\sigma^{\nu\rho}q_\rho}{2m}\gamma^5 F_D. \tag{1.13}$$

In this equation, F_E is the electric form factor, F_M the magnetic form factor, F_A the anapole moment form factor and F_D the electric dipole moment form factor. The magnetic form factor is responsible for the anomalous magnetic moment. It needs to be evaluated at an on-shell momentum transfer, i.e. $q^2 = 0$:

$$F_M(0) = a_\mu.$$

Similarly, evaluating F_E at $q^2 = 0$ gives the electric charge. The factor in front of F_M (or A_2) came from the P^ν vector. This means that when we evaluate a diagram, any parity conserving terms (i.e. without γ^5) proportional to P^ν contribute to a_μ.

First-order contribution

We can now find the first-order QED contribution to the anomalous magnetic moment. It is similar to figure 1.3a but an extra photon is exchanged as shown in figure 1.4. The loop in the diagram contains an unknown momentum labeled k_1, which has to be integrated over.

The matrix element corresponding to figure 1.4 is given by:

$$\frac{i\mathcal{M}^\nu}{(ie)} = \int \frac{\mathrm{d}^4k_1}{(2\pi)^4}\bar{u}(p_2)ie\gamma^\sigma \frac{i(\not{k}_2 + m)}{k_2^2 - m^2 + i\epsilon}\frac{-ig_{\sigma\rho}}{(p_1 - k_1)^2 + i\epsilon}\gamma^\nu \frac{i(\not{k}_1 + m)}{k_1^2 - m^2 + i\epsilon}ie\gamma^\rho u(p_1).$$

We divide out one factor of ie, because this was a general factor in front of Γ^ν in equation 1.10. We use the following γ-relations

$$\begin{aligned} \gamma^\nu\gamma^\rho\gamma_\nu &= -2\gamma^\rho, \\ \gamma^\nu \not{a}\not{b}\gamma_\nu &= 4a \cdot b, \\ \gamma^\nu \not{a}\not{b}\not{c}\gamma_\nu &= -2\not{c}\not{b}\not{a}, \end{aligned}$$

to rewrite the matrix element in a more compact form:

$$\frac{i\mathcal{M}^\nu}{(ie)} = \frac{2ie^2}{(2\pi)^4}\int \mathrm{d}^4k_1 \frac{\bar{u}(p_2)\{\not{k}_1\gamma^\nu\not{k}_2 + m^2\gamma^\nu - 2m(k_1^\nu + k_2^\nu)\}u(p_1)}{[(p_1 - k_1)^2 + i\epsilon][(k_1 + q)^2 - m^2 + i\epsilon][k_1^2 - m^2 + i\epsilon]}. \tag{1.14}$$

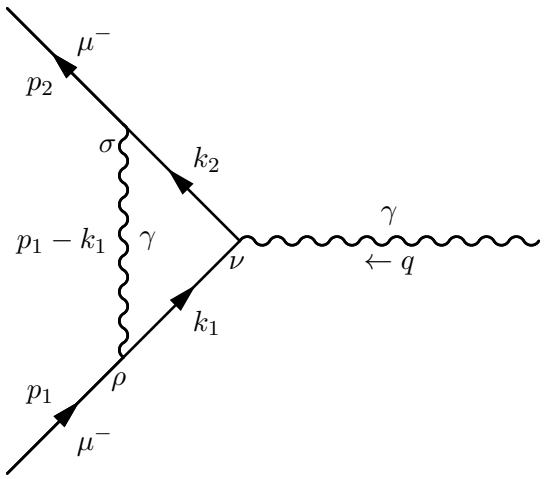

FIGURE 1.4: The 1-loop QED diagram. The greek letters at the vertices are Lorentz indices and the p, k and q represent momenta.

These types of integrals are usually rewritten such that the denominator is in a spherical symmetric form. Feynman parameters are a good way to do this: we look for a new variable l expressed in terms of k, for which the denominator reads like a (degenerate) propagator $[l^2 - \Delta + i\epsilon]^n$. The factor n depends on the number of propagators in the matrix element (here $n = 3$). A simplification of the general formula for finding this denominator is given by [17]:

$$\frac{1}{A_1 A_2 ... A_n} = \int_0^1 \mathrm{d}x_1 \mathrm{d}x_2 ... \mathrm{d}x_n \delta(\sum x_i - 1) \frac{(n-1)!}{[x_1 A_1 + x_2 A_2 ... x_n A_n]^n}. \tag{1.15}$$

By taking $x_1 = x, x_2 = y$ and $x_3 = z$, and choosing $l = k_1 - xp_1 + yq$ and $\Delta = (1-x)^2 m^2 - yzq^2$ we accomplish the desired result:

$$\frac{i\mathcal{M}^\nu}{(ie)} = \frac{4ie^2}{(2\pi)^4} \int \mathrm{d}^4 k_1 \int_0^1 \mathrm{d}x \mathrm{d}y \mathrm{d}z \delta(x+y+z-1) \times \frac{\bar{u}(p_2)\{\not{k}_1 \gamma^\nu \not{k}_2 + m^2 \gamma^\nu - 2m(k_1^\nu + k_2^\nu)\} u(p_1)}{[l^2 - \Delta + i\epsilon]^3}.$$

The numerator and integration variable in the integral in equation 1.14 then have to be rewritten in terms of l. To do this, we make use of the following relations:

$$\begin{aligned} \not{p}_1 u(p_1) &= m u(p_1), \\ \bar{u}(p_2)\not{q} u(p_1) &= 0 \\ (p_1 + q)^2 &= p_2^2, \\ k_1 + q &= k_2, \\ 2p_1 \cdot q + q^2 &= 0, \\ p_1^2 = p_2^2 &= m^2. \end{aligned}$$

We will also discard any term with an odd power of l, as the symmetry of the integral will make these terms vanish. Lastly, any term with $l^\nu l^\rho$ can be rewritten to $\frac{1}{4} g^{\nu\rho} l^2$

due to Lorentz covariance. We then find:

$$\begin{aligned}\frac{i\mathcal{M}^\nu}{(ie)} = \frac{4ie^2}{(2\pi)^4}\int \mathrm{d}^4 l \int_0^1 \mathrm{d}x\mathrm{d}y\mathrm{d}z \frac{\delta(x+y+z-1)}{[l^2-\Delta+i\epsilon]^3} \\ \times \bar{u}(p_2)\Big[\gamma^\nu\big(-\frac{1}{2}l^2 + m^2(1-2x-x^2) + (1-y)(1-z)q^2\big) \\ + (p_2^\nu + p_1^\nu)mx(x-1) + q^\nu m(x-2)(z-y)\Big]u(p_1).\end{aligned} \tag{1.16}$$

We see three distinct terms between the spinors. One is proportional to γ^ν, one is proportional to q^ν and one is proportional to $P^\nu = p_1^\nu + p_2^\nu$. As has been explained, the term multiplied by P^ν is the one that directly contributes to the magnetic form factor and thus a_μ. To arive at the form of equation 1.13, we need to rewrite the term proportional to P^ν with the use of equation 1.12. We then have to evaluate only this part of the integral:

$$F_M(q^2) = 4ie^2 \int \frac{\mathrm{d}^4 l}{(2\pi)^4}\int_0^1 \mathrm{d}x\mathrm{d}y\mathrm{d}z\ \delta(x+y+z-1)\frac{2m^2x(1-x)}{[l^2-\Delta+i\epsilon]^3}. \tag{1.17}$$

We focus first on the integral over l, which only the denominator depends on. To evaluate it, we use a technique called Wick rotation, see [18]. The four vector l is a vector in Minkowski space. Wick rotation rewrites the four vector in a 4-dimensional Euclidean vector and performs the integral in 4-dimensional spherical coordinates. To do this, we define a new variable $l^0 \equiv il_E^0$. We can then evaluate the integral by making use of:

$$\int \frac{\mathrm{d}^4 l}{(2\pi)^4}\frac{1}{[l^2-\Delta]^n} = \frac{i(-1)^n}{(2\pi)^4}\int \mathrm{d}\Omega_4 \int_0^\infty \mathrm{d}l_E \frac{l_E^3}{[l_E^2+\Delta]^n},$$

with $\mathrm{d}\Omega_4$ being the integration measure of a 4-dimensional surface area, resulting in a factor of $2\pi^2$. The other part of the integral over l_E can be evaluated by substituting $a = l_E^2 + \Delta$. It leads to:

$$\frac{i(-1)^n}{(2\pi)^4}\int d\Omega_4 \int_0^\infty \mathrm{d}l_E \frac{l_E^3}{[l_E^2+\Delta]^n} = \frac{i(-1)^n}{(4\pi)^2}\frac{1}{(n-1)(n-2)}\frac{1}{\Delta^{n-2}}.$$

For the denominator in equation 1.17, $n = 3$. This gives us a contribution of $\frac{-i}{2\Delta(4\pi)^2}$ from the l integral. We recall $\Delta = (1-x)^2m^2 - yzq^2$. The integral can now be evaluated at an on-shell momentum transfer ($q^2 = 0$):

$$F_M(0) = \frac{e^2}{8\pi^2}\int_0^1 \mathrm{d}x\mathrm{d}y\mathrm{d}z\ \delta(x+y+z-1)\frac{2m^2x(1-x)}{m^2(1-x)^2} = \frac{e^2}{8\pi^2} = \frac{\alpha}{2\pi}. \tag{1.18}$$

In the last step, the constants are rewritten into the fine-structure constant α.

Remarkably, the final expression is a constant, independent of the mass of the lepton. This means this first-order contribution to the anomalous magnetic moment is exactly the same for all three charged leptons. This is no longer true at higher orders, which causes a difference between the magnetic moments of the three charged leptons.

1.6 Higher-order calculation techniques

The first order QED result, $\frac{\alpha}{2\pi} \approx 0.0011614$, constitutes more than 99% of the total contribution to the anomalous magnetic moment of the muon, as can be seen in equation 1.8. The rest of the contributions come predominantly from higher order QED diagrams, but also EW and QCD diagrams are required to get a precise enough theoretical value for comparison with the experimental value.

Finding an expression for a higher order diagram can become quite difficult. Hence, several techniques to simplify these calculations have been developed. In deriving the expression for the first order QED diagram, we rewrote an integrand until a single useful term could be extracted. A projection operator can do just that; it projects out terms from any matrix element that are required.

Projection operator
For any A_i as defined in equation 1.11, we can define a projection operator $\mathcal{P}_i$ such that:

$$A_i = \text{Tr}[\mathcal{P}_i^\nu \Gamma_\nu]. \tag{1.19}$$

An ansatz for a general projection operator is similar to the covariant decomposition in equation 1.11 but with different coefficients:

$$\mathcal{P}^\nu = (\not{p}_1 + m)\Big[c_1\gamma^\nu + c_2\frac{P^\nu}{2m} + c_3\frac{q^\nu}{2m} + c_4\gamma^\nu\gamma^5 + c_5\frac{q^\nu}{2m}\gamma^5 + ic_6\frac{P^\nu}{2m}\gamma^5\Big](\not{p}_2 + m).$$

The $(\not{p}_1 + m)$ and $(\not{p}_2 + m)$ are necessary to enforce the mass-shell condition for the leptons after taking the trace. More information on this can be found in [16]. We can find expressions for the coefficients c_i by taking the trace of this general projector with the covariant decomposition:

$$\text{Tr}[\mathcal{P}^\nu \Gamma_\nu] = \sum_i^6 g_i A_i.$$

The g_i coefficients are combinations of the c_i coefficients, m, q^2 and d (the number of spacetime dimensions). Writing out the sum gives:

$$\begin{aligned}
\sum_i^6 g_i A_i = {} & A_1\Big[c_1\big(8m^2 + 2dq^2 - 4q^2\big) + c_2\big(8m^2 - 2q^2\big)\Big] \\
& + A_2\Big[c_1\big(8m^2 - 2q^2\big) + c_2\big(8m^2 + \frac{q^4}{2m^2} - 4q^2\big)\Big] \\
& + A_3\Big[c_3\big(2q^2 - \frac{q^4}{2m^2}\big)\Big] \\
& + A_4\Big[c_4\big(2dq^2 + 8m^2 - 8dm^2 - 4q^2\big) + c_5\big(2q^2\big)\Big] \\
& + A_5\Big[c_4\big(-2q^2\big) + c_5\big(\frac{q^4}{2m^2}\big)\Big] \\
& + A_6\Big[c_6\big(\frac{q^4}{2m^2} - 2q^2\big)\Big].
\end{aligned}$$

For the anomalous magnetic moment, we need $\mathcal{P}_2^\nu$. This is found by setting $g_2 = 1$ and every $g_i = 0\,\forall\, i \neq 2$. We note that g_2 is a function of the coefficients c_1 and c_2 and note that these coefficients further appear in g_1. Hence, we need to find expressions

for c_1 and c_2 such that $g_1 = 0$ and $g_2 = 1$. We find:

$$c_1 = c_2 \frac{2q^2 - 8m^2}{2dq^2 + 8m^2 - 4q^2}, \qquad c_2 = \frac{2(d-2)m^2q^2 + 8m^4}{(d-2)q^2(q^2-4m^2)^2}.$$

The projector for the magnetic moment is then given by substituting c_1 and c_2 into the general projection operator which yields [19]:

$$\mathcal{P}_2^\nu = (\not{p}_1 + m)\frac{2m^2}{(d-2)q^2(q^2-4m^2)}\Big(\gamma^\nu + \frac{(d-2)q^2 + 4m^2}{q^2-4m^2}\frac{P^\nu}{2m}\Big)(\not{p}_2 + m). \tag{1.20}$$

Mass expansion

Another technique, often used in conjunction with the projection operator, is applying a mass expansion. This can be done when a particle inside the loop of a diagram is massive compared to the masses of the incoming and outgoing particle. For the anomalous magnetic moment, we only evaluate diagrams with an incoming and outgoing muon. Hence, for any diagram where there is a particle in the loop heavier than 0.1 GeV, we can apply this technique. This will often be the case in electroweak diagrams and most supersymmetry diagrams [20].

Let us look at the diagram in figure 1.5 to exemplify this technique. We see two scalar boson particles denoted by A and a fermion particle denoted by B and assume $M_A, M_B \gg m_\mu, p_1, p_2$. Let us denote the vertex couplings as $n^{\text{in,out}}_{AB\mu}$ and $n^\nu_{AA\gamma}$ and the loop momentum by l. We can then find Γ^μ for this diagram:

$$\Gamma^\nu = \int \frac{d^4l}{ie}\frac{n^{\text{out}}_{AB\mu}n^\nu_{AA\gamma}(\not{l} + M_B)n^{\text{in}}_{AB\mu}}{[(p_1-l)^2 - M_A^2](l^2 - M_B^2)[(p_2-l)^2 - M_A^2]}.$$

We can now apply the mass expansion. This means we assume $[(p_1 - l)^2 - M_A^2] \simeq [l^2 - M_A^2]$. In doing so, we neglect a part of the denominator for which we have to correct via a Taylor expansion. We omit the couplings and numerical factors, as they do not influence the integral. The result is:

$$\Gamma \propto \int d^4l \frac{\not{l} + M_B}{(l^2 - M_B^2)(l^2 - M_A^2)^2} \cdot \Big[1 + \frac{2l\cdot p_1}{l^2 - M_A^2} + \frac{2l\cdot p_2}{l^2 - M_A^2} + \text{H.O.}\Big].$$

We note that, especially in the context of electroweak and supersymmetry diagrams, these vertices can be dependent on the chirality of the particles, adding a factor of $(1 \pm \gamma^5)$. This effectively projects out either the M_B or the $\not{l}$ from the numerator. Regardless of which term remains, one can group even and odd terms, since any integral with an odd amount of l factors in the numerator vanishes. The resulting integral will be of the form (up to whichever order you continue the expansion):

$$\Gamma^\mu \propto \int d^4l \frac{l^{(2m)}}{(l^2 - M_B^2)(l^2 - M_A^2)^n},$$

with $n > 2m$. This integral can be evaluated for $n = 1$ and $m = 0$. For higher orders of m, one can introduce an extra M_A^2 term to cancel it with the equal term in the denominator and any $n > 1$ integral can be found by taking derivatives of the $n = 1$ integral with respect to M_A^2. Similar expansions can be made for other types of interactions or whenever only one of the (different) particles is heavy.

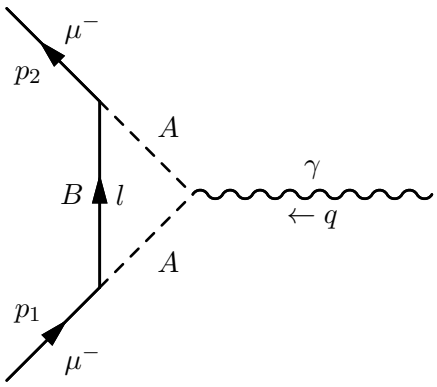

FIGURE 1.5: A theoretical diagram with heavy particles A and B inside the loop. The momentum of particle B is labeled by l.

1.7 Higher order QED, EW and strong contributions

QED contributions

With the techniques of the previous section, a lot of progress has been made on higher order QED calculations. Even so, computer techniques have to be used to reach a theoretical precision comparable to the experimental one. Up to 5 loop orders (12672 diagrams) have been calculated, using numerical integration techniques, see [21]. The total QED contribution up to the fifth order is given by [22]:

$$a_\mu^{\mathrm{QED}} = 116584718.92(0.03) \cdot 10^{-11}. \tag{1.21}$$

The largest part of the uncertainty is caused by the uncertainty in α. Smaller uncertainties originate from the ratio of lepton masses and the uncertainty of the employed numerical-integration techniques.

EW contribution

With the help of equation I.1, we can estimate the electroweak contributions to the anomalous magnetic moment. To do this, we use the mass of the heaviest particle in the diagram as M in the equation. In the case of the diagram in figure 1.6b this would be the W boson. We find the electroweak contributions to be of order $4 \cdot 10^{-7}$ weaker than the first-order QED contribution. However, due to the precision of both the QED calculations and the experimental measurements, we have to take these diagrams into account anyway.

If one calculates both first order diagrams given in figure 1.6, their contribution would be $194.8 \cdot 10^{-11}$ [23]. Higher orders will in general contribute less, due to each order scaling with another order of the electroweak coupling constant. However, here it turns out that the two-loop contribution is surprisingly large and negative: $-41.2 \cdot 10^{-11}$ [24]. It thus provides a non-negligible correction to the first order result. This is due to the Higgs Boson coming into play at two loops and higher, along with corrections to the first-order EW diagrams. A diagram that can be considered a correction to a first-order EW diagram, would be one where an extra photon is exchanged between the incoming and outgoing muon. This would be considered a QED correction to the first-order EW diagrams. If a Z boson would be exchanged, it would be an EW correction. These second-order contributions can be summarised

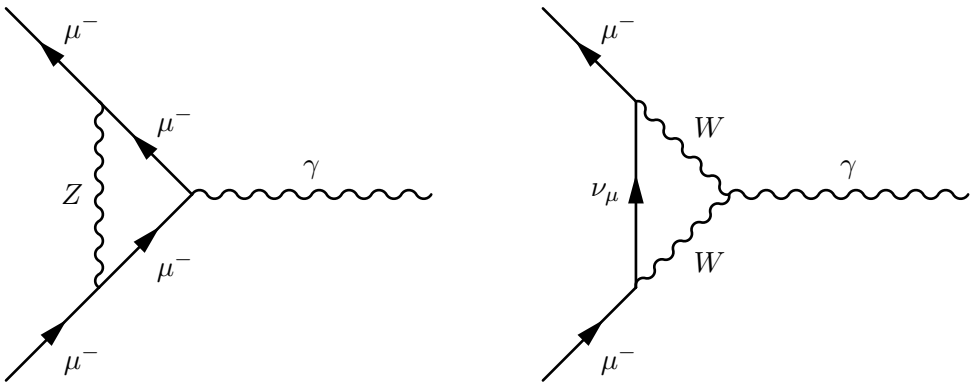

(A) Electroweak 1-loop diagram with a Z-boson exchange.

(B) Electroweak 1-loop diagram with two W-bosons and a muon neutrino exchange.

FIGURE 1.6: The two 1-loop diagrams which add the largest Electroweak contribution to the anomalous magnetic moment of the muon.

by making use of the projection operator and the mass expansion [20] [25]:

$$\begin{aligned} \delta a_\mu^{\text{2L EW}} &= \frac{5}{3}\frac{G_\mu m_\mu^2}{8\pi^2\sqrt{2}}\frac{\alpha}{\pi}\Big(c_L \log\frac{m_\mu^2}{m_W^2} + c_0\Big), \\ c_L &= \frac{1}{30}\big[107 + 23(1 - 4\sin^2\theta_W)^2\big], \end{aligned} \tag{1.22}$$

where θ_W is the Weinberg angle, m_W the mass of the W boson and G_μ is the Fermi constant in terms of the muon lifetime, see [26]. The c_0 term is quite complicated, but is roughly equal to 10% of the log term and thus this correction can at first glance be approximated by evaluating only the log term ($\approx -22.9 \cdot 10^{-11}$).

Three or higher loop orders have not been calculated yet, but are estimated to be negligible at the moment; their contribution is smaller than the current experimental and theoretical precision. The total electroweak contribution is:

$$a_\mu^{\text{EW}} = \frac{5}{3}\frac{G_\mu m_\mu^2}{8\pi^2\sqrt{2}}\Big(1 + \frac{\alpha}{\pi}c_L \log\frac{m_\mu^2}{m_W^2} + \frac{\alpha}{\pi}c_0\Big) = 153.6(1.0)\cdot 10^{-11}. \tag{1.23}$$

The main source of uncertainty is due to the diagrams with a quark loop at two loop orders.

QCD contributions

The largest uncertainty in the theoretical calculation of the anomalous magnetic moment is due to contributions of diagrams involving the strong coupling, usually referred to as hadronic contributions. These involve diagrams with quarks and gluons, and are mainly a problem due to the non-perturbative nature of the strong coupling at low energy scales. Unfortunately, we are interested in exactly these scales by definition ($q^2 = 0$). We therefore need a combination of both traditional perturbative, and non-perturbative techniques. As a result, the uncertainties are large. The total

hadronic contribution is calculated (partially up to third order) to be [27]:

$$a_\mu^{\text{hadr}} = 6939(39)(7) \cdot 10^{-11} + 19(26) \cdot 10^{-11}. \tag{1.24}$$

The largest contribution comes from second-order diagrams as seen in figure 1.7 and is determined by combining experimental measurements with a dispersive relation running down from higher energies [28]. This means the uncertainty will be partly experimental and partly due to perturbative QCD at higher energies. The second contribution is from all the higher-order diagrams that have been evaluated so far by a technique called hadronic light-by-light scattering, see [29]. The uncertainty comes from the use of this technique.

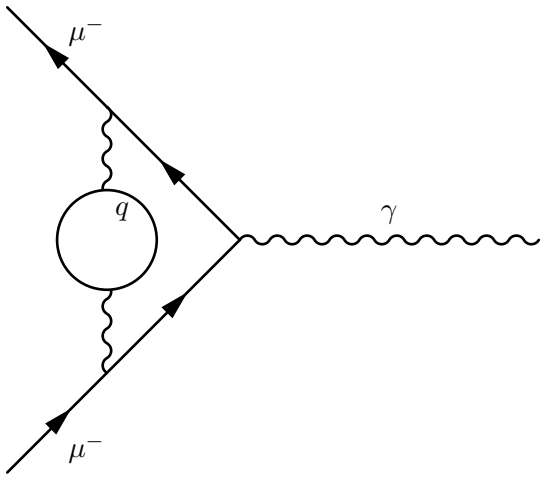

FIGURE 1.7: The highest contributing QCD diagram. The q can be any quark.

1.8 Total theoretical contribution

We have now listed all the currently known SM contributions to the anomalous magnetic moment. The uncertainty on the theoretical value is, at present, better than the experimental uncertainty, but both are still actively being improved by collaborations from all over the world. The total theoretical contribution is given by summing 1.21, 1.23 and 1.24:

$$a_\mu^{\text{SM}} = 116591823(1)(34)(26) \cdot 10^{-11}. \tag{1.25}$$

The 10^{-13} uncertainty made in calculating the QED contributions has been omitted in this value with respect to the 10^{-11} EW and 10^{-10} QCD uncertainties. For simplicity, the uncertainties listed here have been added quadratically for the total theoretical uncertainty.

The 3.3σ deviation between experiment and theory is now apparent when computing the difference: $\Delta a_\mu = a_\mu^{\text{SM}} - a_\mu^{\text{exp}} = -268(48)(63) \cdot 10^{-11}$. Here, the first uncertainty is due to theory and the second due to experiment. The new experiment mentioned in chapter 1.3 will aim to reduce the last uncertainty such that it will be smaller than the theoretical uncertainty.

Chapter 2

Supersymmetry

The deviation between experiment and theory of the anomalous magnetic moment is not yet significant enough to warrant new physics, but might soon be. It will then become a shortcoming of the SM. There are many more shortcomings within the SM which already require us to look at theories for new physics, usually referred to as Beyond the Standard Model (BSM) theories. Such BSM theories aim to solve or shed light on:

- The matter-antimatter asymmetry problem:
  According to the theory of the Big Bang, particles and antiparticles should have been created in equal amounts, or should have annihilated each other until only pure energy was left. However, we observe more matter than anti-matter. A possible explanation is that CP-violating processes create an imbalance. In the SM the amount of CP violation is not big enough to explain the observed imbalance. A BSM theory could include the additional CP violation that is needed.

- The origin of neutrino masses:
  The mechanism for giving neutrinos mass is not fully specified within the SM. Initially, there was no mass term within the SM for neutrinos. However, neutrino experiments show oscillations between neutrino flavours, implying a neutrino to be in a mass eigenstate of multiple flavours. This means at least two of the three neutrinos need to have a mass. The SM can provide mass to the neutrinos but does not exploit all possibilities and does not explain the smallness of these masses. If a BSM theory could provide a clear-cut mechanism for providing the neutrinos with mass, it would solve one of the unanswered questions within the SM.

- The origin of dark matter:
  The problem of dark matter is perhaps the best known. It has been postulated in the early 1900's and was popularised by Vera Rubin in the 1970's as being responsible for the experimentally inferred missing mass in galaxies or galaxy clusters compared to what is visible. Many physicists accept the idea of dark matter, but not everyone agrees on what it is supposed to be. If the SM would be extended by a BSM theory, one could think of dark matter as a particle that evades (almost) all detection through conventional means.

- Fine-tuning problem of the Higgs boson:
  The Higgs mass has been measured to be roughly 125 GeV. However, once we allow for a new scale of physics, there are self-energy corrections to the Higgs mass that scale with the square of the scale of new physics. We already know that scale has to be at least an order of magnitude larger than the mass of the Higgs boson. This means a BSM theory that wants to solve this problem has to

introduce a mechanism to counteract this. One example could be to introduce counter terms. There is currently no mechanism within the SM itself to do this, which means the higher order corrections due to higher scale new physics are a lot larger than the Higgs mass itself. Most physicists agree that a theory which doesn't involve arbitrarily large corrections would be preferred.

- Gauge coupling unification:
  When plotting the three gauge couplings within the SM versus energy, we see them nearly reaching a unified point at a high energy scale. They just miss, which might be due to the fact that the SM is not a complete theory. This is not actually a problem of the SM and the force of gravity is left out as it doesn't come near this unified point, but nonetheless, physicists argue that theories that unify these gauge couplings at high energy are worth pursuing.

- And more:
  As mentioned above, this list is not complete. There are other open questions and it is not certain that a generic BSM theory could solve all problems simultaneously. Many of these lists will, for example, not include the anomalous magnetic moment. We will mention it here because it is the topic of this work, but it is not considered a problem of the SM yet, in view of the current 3.3σ significance. More of these less significant discrepancies are present in the SM, next to more significant ones, like gravity and dark energy.

In this thesis we will consider one BSM theory in particular: the pMSSM. This is a specific implementation of Supersymmetry (SUSY), which adds new symmetries to the already existing ones of the SM. In the pMSSM, a symmetry is added in such a way that the number of new parameters is minimized. A SUSY theory could be able to explain quite a number of the aforementioned problems, like dark matter, the fine-tuning problem, gauge coupling unification and more.

This added symmetry by SUSY is one that transforms fermions into bosons and vice versa. It can also be thought of as adding a symmetry between the mass (matter) and interaction (force) terms of the Lagrangian. This requires the addition of new particles to the SM theory, for each fermion a new boson and vice versa. These new particles are called the superpartners of the SM particles. The bosonic superpartners share the same name as the SM fermions, but with an 's' attached to the front, i.e. smuon is the superpartner of the muon. The fermionic superpartners are renamed by changing the end of the boson name to 'ino', i.e. photino becomes the superpartner of the photon.

2.1 The pMSSM

The MSSM attempts to minimize the number of new particles [30]. Still, it leads to over a hundred free parameters due to the unknown mechanism for symmetry breaking.

Two of the core principles of the MSSM are R-parity and the expansion of the Higgs sector. R-parity is a new parity introduced by supersymmetry, which adds a new conserved multiplicative quantum number. This quantum number is -1 for all supersymmetric particles and 1 for all SM particles.

The Higgs sector gets expanded as a new separate Higgs doublet is required to give mass to the down-type quarks versus the up-type quarks. Another reason is that chiral anomalies will occur if one uses only one Higgs boson doublet, see [31]. Both of these Higgs doublets get superpartners as well, which eventually leads to the requirement of 5 different Higgs bosons in the MSSM.

The phenomenological MSSM (pMSSM) consists of a set of constraints that intend to lower the number of free parameters of the MSSM, based on assumptions motivated by experiments. The added particle content of the (p)MSSM is summarised in table 2.1. Note that the electric charge of all superpartners is equal to their SM counterparts found in table 1.1 and thus has been excluded from the table.

Two important constraints placed on the MSSM, to create the pMSSM, are:

- There is a degeneracy between the first and second generation sfermions. For example, the mass of the selectron and the mass of the smuon will be the same.
- The trilinear couplings of the first and second generation are set to zero. These trilinear couplings are added to the SUSY Lagrangian after symmetry breaking and quantify the couplings between the Higgs particles and the sleptons and squarks. In the pMSSM, only the trilinear couplings for the stop, sbottom and stau particles remain.
- Any terms that appear in the SUSY lagrangian that add new forms of CP-violation are set to 0.

SUSY particles	spin-0	spin-$\frac{1}{2}$
squarks (3 families)	$(\tilde{u}_L\ \tilde{d}_L)$ $\tilde{u}_R^\dagger$ $\tilde{d}_R^\dagger$	
sleptons (3 families)	$(\tilde{\nu}_L\ \tilde{e}_L)$ $\tilde{e}_R^\dagger$	
higgsinos		$(\tilde{H}_u^+\ \tilde{H}_u^0)$ $(\tilde{H}_d^0\ \tilde{H}_d^-)$
gluino		$\tilde{g}$
wino		$\tilde{W}^\pm\ \tilde{W}^0$
bino		$\tilde{B}^0$

TABLE 2.1: The added particle content of the MSSM.

2.2 Symmetry breaking

The symmetry that SUSY introduces, predicts all supersymmetric particle masses to be equal to their SM counterparts. This means that, for example, the smuon should have a mass of 0.105658 GeV, equal to that of the muon. If that would be the case, we would have expected to have already found these particles at particle collider

experiments such as the LHC.

Presently, no supersymmetric particle has been discovered and the Higgs mass has been determined to be roughly 125 GeV. As such, one has to introduce a mechanism in order for the supersymmetric masses to be different from their SM counterparts, i.e. SUSY needs to be a broken symmetry.

The exact mechanism behind the symmetry breaking is not known and therefore we add it in a general way, see [32]. This introduces over a hundred free parameters to the SUSY Lagrangian.

In the context of the anomalous magnetic moment, we find another reason for symmetry breaking: if SUSY would be unbroken, the anomalous magnetic moment would exactly vanish. The SUSY particles would cause corrections to the anomalous magnetic moment equal to the SM corrections but with a relative minus sign [33].

2.3 The free parameters of the theory

3 Higgs parameters	Gaugino parameters and trilinear couplings	10 Mass Parameters
$\tan\beta$	M_1 A_t	$M_{\tilde{e}}^L$ $M_{\tilde{\tau}}^L$
μ	M_2 A_b	$M_{\tilde{e}}^R$ $M_{\tilde{\tau}}^R$
m_A	M_3 A_τ	$M_{\tilde{u}}^L$ $M_{\tilde{t}}^L$
		$M_{\tilde{u}}^R$ $M_{\tilde{t}}^R$
		$M_{\tilde{d}}^R$ $M_{\tilde{b}}^R$

TABLE 2.2: The free parameters of the pMSSM.

The pMSSM has 19 free parameters. The 19 free parameters can be divided into categories: the majority of parameters will be sfermion mass parameters and then there will be three Higgs parameters, three trilinear couplings and three gaugino soft SUSY breaking terms, see table 2.2. From these parameters, the mass spectrum of the pMSSM can be determined, as can the branching ratios of all particle processes and the anomalous magnetic moment.

The Higgs parameters are $\tan\beta$, μ and m_A. The μ parameter is the only SUSY respecting parameter. In a generic SUSY theory it can become complex, but due to all extra CP-violating terms being set to 0 in the pMSSM, μ has to be real. Similarly, the soft SUSY breaking parameters A_t, A_b, A_τ, M_1, M_2 and M_3 cannot be complex because of this.

The 10 mass parameters cover all sfermion masses in the pMSSM. The $M_{\tilde{e}}^L$ parameter is the mass term for the left-handed selectron and smuon and $M_{\tilde{e}}^R$ for the same

right-handed particles. The selectron and smuon do not mutually mix, but the same family left-handed and right-handed particles do. The stau particle is not degenerate with the other two sleptons, so different mass parameters are needed for it, namely $M_{\tilde{\tau}}^L$ for the left-handed stau and $M_{\tilde{\tau}}^R$ for the right-handed. For the squarks a similar approach is used, but one needs to differentiate between the up and down squarks. The parameter $M_{\tilde{u}}^L$ gives the masses for the up, down, strange and charm squarks in the left-handed doublets and $M_{\tilde{u}}^R$ and $M_{\tilde{d}}^R$ give mass to the for right-handed up and charm, and down and strange squark respectively.

Renormalisation group equations
The free parameters described above are input parameters for a specific pMSSM mass spectrum. These input parameters are defined at the general supersymmetry scale commonly referred to as M_{SUSY}, which is usually set to $\sqrt{M_{\tilde{t}}^L M_{\tilde{t}}^R}$. To find out, for example, what the branching ratio of a certain decay is at the m_Z scale (the energy scale corresponding to the mass of the Z-boson), one has to 'run' these input parameters down from the M_{SUSY} scale to the m_Z scale. This is done by the renormalisation group equations.

These equations form 19 coupled differential equations, one for each of the free parameters. The renormalisation group equations for the SM couplings also get slightly altered. We will not give futher details here, but for more information see [34]. It is important to note however, that when varying for example m_A while keeping the other pMSSM parameters constant, one might still see the other parameters change at the m_Z scale, as they get influenced by this change in m_A during their running.

2.4 Parameter mixing

We will now discuss the parameters that are relevant for the supersymmetric contribution to the anomalous magnetic moment, for more information see [35]. We will look at the three categories: the Higgs sector, gauginos and sfermions. Each of these categories has accompanying mixing matrices coming from the Lagrangian terms due to symmetry breaking.

2.4.1 Higgs sector

Let us start with the extended Higgs sector in the pMSSM. As mentioned above, there are two Higgs doublets in the pMSSM with opposite hypercharge. They form 8 mass eigenstates after spontaneous symmetry breaking. Three of these are the unphysical goldstone bosons (G^0 and $G^{\pm}$) which will be used to give mass to the Z^0 and $W^{\pm}$ bosons. The other 5 become physical Higgs bosons. Two of these are CP-even scalars, denoted by h_0 and H_0, and A_0 is the CP-odd scalar. The other two Higgs bosons are the charged ones, $H^{\pm}$. To arrive at the mass eigenstates one has to parameterise the doublets as

$$H_d = \begin{pmatrix} \frac{1}{\sqrt{2}}(v_d + \phi_1^0 - iN_1^0) \\ -\phi_1^- \end{pmatrix}, \qquad H_u = \begin{pmatrix} \phi_2^+ \\ \frac{1}{\sqrt{2}}(v_u + \phi_2^0 + iN_2^0) \end{pmatrix}.$$

The H_d doublet has a hypercharge of -1. The H_u doublet has a hypercharge of 1. From these one can find the mass eigenstates:

$$\begin{pmatrix} H_0 \\ h_0 \end{pmatrix} = \begin{pmatrix} \cos\alpha & \sin\alpha \\ -\sin\alpha & \cos\alpha \end{pmatrix} \begin{pmatrix} \phi_1^0 \\ \phi_2^0 \end{pmatrix},$$
$$\begin{pmatrix} G_0 \\ A_0 \end{pmatrix} = \begin{pmatrix} \cos\beta & \sin\beta \\ -\sin\beta & \cos\beta \end{pmatrix} \begin{pmatrix} N_1^0 \\ N_2^0 \end{pmatrix},$$
$$\begin{pmatrix} G^\pm \\ H^\pm \end{pmatrix} = \begin{pmatrix} \cos\beta & \sin\beta \\ -\sin\beta & \cos\beta \end{pmatrix} \begin{pmatrix} \phi_1^\pm \\ \phi_2^\pm \end{pmatrix}.$$

The mixing angle α is related to the angle β and the mass m_A of A_0 at tree level:

$$\frac{\tan 2\alpha}{\tan 2\beta} = \frac{m_A^2 + m_Z^2}{m_A^2 - m_Z^2}. \tag{2.1}$$

The m_Z parameter represents the Z-boson mass and β is a free parameter. It is given by the inverse tangent of the ratio of vacuum expectation values of the Higgs doublets, which cannot both be zero due to electroweak symmetry breaking:

$$\frac{v_u}{\sqrt{2}} = \langle H_u \rangle, \qquad \frac{v_d}{\sqrt{2}} = \langle H_d \rangle, \qquad \implies \tan\beta = \frac{v_u}{v_d}.$$

The parameter m_A determines the mass of the CP-odd Higgs scalar A_0.

2.4.2 Gauginos

The gluino is a colour octet fermion and as such, does not mix with any of the other gauginos. It is unique in that regard and therefore has its own gaugino soft SUSY breaking parameter, called M_3, which is in general only connected to the other parameters via renormalisation group equations.

The other gaugino soft-SUSY breaking parameters in the pMSSM fermion sector are M_1 (for $\tilde{B}$) and M_2 (for $\tilde{W}$). These do mix due to $SU(2)_L$ symmetry breaking. This leads to mass eigenstates for these sparticles. The mass eigenstates for the neutral (charged) pMSSM fermions are called neutralinos (charginos). There are only two charginos, in the same sense as there is only one W-boson. Each positively charged chargino has a negatively charged counterpart of equal mass, similarly to the W boson. This means that the gauge eigenstates ($\tilde{H}_u^+$, $\tilde{W}^\pm$, $\tilde{H}_d^-$) combine to form the mass eigenstates ($\tilde{\chi}_1^\pm$, $\tilde{\chi}_2^\pm$).

To find the mass eigenstates of the charginos we use the unitary matrices for the differently charged fermions, labelled V and U. The mass eigenstates and the gauge eigenstates are linked by these matrices:

$$\begin{pmatrix} \tilde{\chi}_1^+ \\ \tilde{\chi}_2^+ \end{pmatrix} = V \begin{pmatrix} \tilde{W}^+ \\ \tilde{H}_u^+ \end{pmatrix}, \qquad \begin{pmatrix} \tilde{\chi}_1^- \\ \tilde{\chi}_2^- \end{pmatrix} = U \begin{pmatrix} \tilde{W}^- \\ \tilde{H}_d^- \end{pmatrix}.$$

The unitary matrices V and U are defined such that:

$$U^* C V^{-1} = \begin{pmatrix} m_{\tilde{\chi}_1^\pm} & 0 \\ 0 & m_{\tilde{\chi}_2^\pm} \end{pmatrix}, \quad \text{with } C = \begin{pmatrix} M_2 & \sqrt{2} m_W \sin\beta \\ \sqrt{2} m_W \cos\beta & \mu \end{pmatrix}. \tag{2.2}$$

The matrix C is the mass matrix of the charginos. We see that M_2, μ and β directly influence the mass of the charginos. The convention is that the lightest chargino is $\tilde{\chi}_1^\pm$.

The higgsinos, wino and bino gauge-eigenstates mix into four mass eigenstates called neutralinos. The mass matrix Y of the neutralino sector is given by:

$$Y = \begin{pmatrix} M_1 & 0 & -m_Z \cos\beta \sin\theta_W & m_Z \sin\beta \sin\theta_W \\ 0 & M_2 & m_Z \cos\beta \cos\theta_W & -m_Z \sin\beta \cos\theta_W \\ -m_Z \cos\beta \sin\theta_W & m_Z \cos\beta \cos\theta_W & 0 & -\mu \\ m_Z \sin\beta \sin\theta_W & -m_Z \sin\beta \cos\theta_W & -\mu & 0 \end{pmatrix}. \tag{2.3}$$

The neutralino mass eigenstates can then be found in analogy to the chargino case by introducing a unitary matrix N:

$$N^* Y N^{-1} = \begin{pmatrix} m_{\tilde{\chi}_1^0} & 0 & 0 & 0 \\ 0 & m_{\tilde{\chi}_2^0} & 0 & 0 \\ 0 & 0 & m_{\tilde{\chi}_3^0} & 0 \\ 0 & 0 & 0 & m_{\tilde{\chi}_4^0} \end{pmatrix}, \quad \text{with} \quad \begin{pmatrix} \tilde{\chi}_1^0 \\ \tilde{\chi}_2^0 \\ \tilde{\chi}_3^0 \\ \tilde{\chi}_4^0 \end{pmatrix} = N \begin{pmatrix} \tilde{B}^0 \\ \tilde{W}^0 \\ \tilde{H}_d^0 \\ \tilde{H}_u^0 \end{pmatrix}. \tag{2.4}$$

The lightest supersymmetric particle (LSP) is stable due to R-parity conservation. If the pMSSM were to solve the dark matter problem, we may assume in addition that the LSP is neutral. Hence, the lightest of the neutralinos is a DM candidate. The convention is that the lightest neutralino is $\tilde{\chi}_1^0$ and the heaviest $\tilde{\chi}_4^0$.

2.4.3 Sfermions

As mentioned before, we require diagonal mass matrices to turn off flavour mixing for the first two families of MSSM bosons. There is however, mixing between the left and right handed states of the sfermions per family. This is parameterised by the matrix:

$$m_{\tilde{f}}^2 = \begin{pmatrix} m_f^2 + (M_{\tilde{f}}^L)^2 + \Delta_{\tilde{f}_L} & m_f (A_f - \mu\{\cot\beta, \tan\beta\}) \\ m_f (A_f - \mu\{\cot\beta, \tan\beta\}) & m_f^2 + (M_{\tilde{f}}^R)^2 + \Delta_{\tilde{f}_R} \end{pmatrix}, \tag{2.5}$$

where all parameters are taken to be real. The $\{\cot\beta, \tan\beta\}$ correspond to $\{\tilde{u}, \tilde{d}\,/\tilde{e}\}$ and all higher families, meaning all down type squarks and sleptons will have $\tan\beta$ in their respective mixing matrix. The $M_{\tilde{f}}^{L,R}$ parameters denote the mass of the sfermion in question. The A_f are the soft trilinear couplings between sfermions and Higgs bosons and, as mentioned, are set to 0 for the first two families in the pMSSM. Therefore, for cases when μ is of the order of the slepton and Z-boson masses or smaller, the off-diagonal terms in the mixing matrix are negligible in comparison to

the diagonal terms. The Δ terms are given by:

$$\Delta_{\tilde{f}_L} = M_Z^2 \cos(2\beta)(I_3^f - Q^f \sin^2\theta_W)$$
$$\Delta_{\tilde{f}_R} = M_Z^2 \cos(2\beta) Q^f \sin^2\theta_W,$$

where I_3^f is the weak isospin and Q_f the fractional charge of the corresponding SM fermion. The diagonal entries in the mixing matrix are usually approximated by the squares of $M_{\tilde{f}}^L$ and $M_{\tilde{f}}^R$, which are the free parameters in the theory.

The mass eigenstates of the sfermions can be found in a similar way as described above for the neutralinos and charginos. We conclude this chapter by showing the diagonalisation for the smuon mass matrix as an example here:

$$X^* m_{\tilde{\mu}}^2 X^{-1} = \begin{pmatrix} m_{\tilde{\mu}_1} & 0 \\ 0 & m_{\tilde{\mu}_2} \end{pmatrix}, \text{ with } \begin{pmatrix} \tilde{\mu}_1 \\ \tilde{\mu}_2 \end{pmatrix} = X \begin{pmatrix} \tilde{\mu}_L \\ \tilde{\mu}_R \end{pmatrix}, \tag{2.6}$$

with X an orthogonal matrix. We approximate $A_{\tilde{\mu}} = 0$ and set $m_\mu = 0$ on the diagonal entries. Next to that, we set $\Delta_f = 0$. This is a valid approximation as long as $M_{\tilde{e}}^L$ is not too small. The expression for X will then only depend on μ, $\tan\beta$, $M_{\tilde{e}}^L$ and $M_{\tilde{e}}^R$. The entries of the X matrix are then given by:

$$\begin{aligned} X_{11} &= \cos\left(\frac{1}{2}\arctan\left(\frac{-2m_{\tilde{\mu},12}^2}{-m_{\tilde{\mu},11}^2 + m_{\tilde{\mu},22}^2}\right)\right) = X_{22}, \\ X_{12} &= \sin\left(\frac{1}{2}\arctan\left(\frac{-2m_{\tilde{\mu},12}^2}{-m_{\tilde{\mu},11}^2 + m_{\tilde{\mu},22}^2}\right)\right) = -X_{21}, \end{aligned} \tag{2.7}$$

where a parameter $m_{\tilde{\mu},ij}^2$ corresponds to the (i,j) element of the matrix in equation 2.5. The mass eigenstates of the smuons can then be found in the following way:

$$\begin{aligned} m_{\tilde{\mu}_1} &= \sqrt{\frac{1}{2}[(M_{\tilde{\mu}}^L)^2 + (M_{\tilde{\mu}}^R)^2] - \frac{1}{2}\sqrt{[(M_{\tilde{\mu}}^L)^2 - (M_{\tilde{\mu}}^R)^2]^2 + 4(m_{\tilde{\mu},12}^2)^2}}, \\ m_{\tilde{\mu}_2} &= \sqrt{\frac{1}{2}[(M_{\tilde{\mu}}^L)^2 + (M_{\tilde{\mu}}^R)^2] + \frac{1}{2}\sqrt{[(M_{\tilde{\mu}}^L)^2 - (M_{\tilde{\mu}}^R)^2]^2 + 4(m_{\tilde{\mu},12}^2)^2}}. \end{aligned} \tag{2.8}$$

As with the neutralinos and charginos, the convention is such that the first smuon is always the lowest in mass.

Chapter 3

Supersymmetric contributions to the anomalous magnetic moment

In the last chapter, we have introduced SUSY and specifically the pMSSM. We will now see what impact the pMSSM has on the anomalous magnetic moment. Besides the extra pMSSM diagrams that become relevant, the diagrams discussed in chapter 1.7 containing a Higgs boson will change.

The contribution of any SUSY diagram can be estimated before explicitly evaluating the diagrams. Recall from equation I.1 that we estimate that any diagram will scale with M_{SUSY}^{-2}. This would mean that the SUSY contributions are heavily suppressed. There are however down-type Yukawa couplings which can enhance the contributions significantly. Diagrams containing these couplings are therefore expected to contribute to Δa_μ. Another thing to note is that any SUSY diagram will scale with at least one factor of m_μ.

3.1 First-order diagrams

There are only two first-order pMSSM diagrams. The muon couples to one charged and one neutral supersymmetric particle due to the conservation of R-parity and charge. Furthermore, due to lepton number conservation, one of these supersymmetric particles has to be a smuon or a muon sneutrino. If the lepton number is carried by a smuon, then the other particle is a neutralino. If it is carried by a muon sneutrino, the other particle is a chargino.

We encapsulate all neutralino contributions into a single diagram. The same holds for the chargino contributions. Both diagrams are shown in figure 3.1. Applying the Feynman rules found in [36] and then the projection operator and mass expansion as described in chapter 1.6, one finds for the neutralino contribution [37]:

$$\begin{aligned}\delta a_\mu^{\tilde{\chi}^0} = \frac{m_\mu}{16\pi^2}\sum_{i=1}^{4}\sum_{m=1}^{2}\Big\{&-\frac{m_\mu}{12m_{\tilde{\mu}_m}^2}(\mid n_{im}^L\mid^2+\mid n_{im}^R\mid^2)F_1^N\left(\frac{m_{\tilde{\chi}_i^0}^2}{m_{\tilde{\mu}_m}^2}\right)\\&+\frac{1}{3}\frac{m_{\tilde{\chi}_i^0}}{m_{\tilde{\mu}_m}^2}\mathrm{Re}[n_{im}^L n_{im}^R]F_2^N\left(\frac{m_{\tilde{\chi}_i^0}^2}{m_{\tilde{\mu}_m}^2}\right)\Big\}.\end{aligned} \tag{3.1}$$

Before we list exact expressions for the terms we see in this equation, we will sketch a general interpretation first.

The sum with index i runs over all neutralino mass eigenstates. The sum with index m runs over all smuon mass eigenstates, where $m_{\tilde{\mu}_m}$ is the respective smuon mass. The n_{im} terms are couplings between the specific neutralino and smuon state, separated into 3 different cases: either the coupling is between two left-handed particles, two right-handed particles or a left and right-handed particle. Note that in writing the contribution in this way, certain physical parameters will be hidden inside the couplings, such as the linear dependence on α_{em} for first-order processes. The F_i^N are the loop functions, they follow from the mass expansion and depend on the mass ratio of the two SUSY particles in the loop.

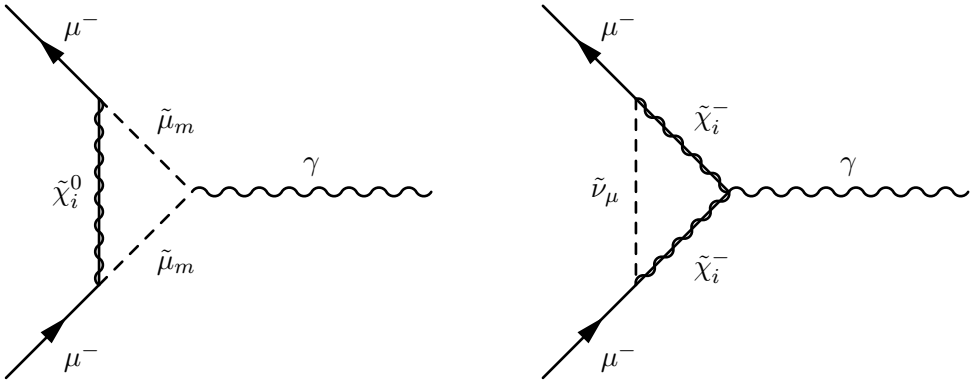

(A) The neutralino loop diagram. (B) The chargino loop diagram.

FIGURE 3.1: The only two possible first-order pMSSM diagrams which contribute to the anomalous magnetic moment of the muon.

The exact expressions for the loop functions and the couplings are as follows:

$$\begin{aligned} n_{im}^L &= \frac{1}{\sqrt{2}}(g_1 N_{i1} + g_2 N_{i2}) X_{m1}^* - y_\mu N_{i3} X_{m2}^*, \\ n_{im}^R &= \sqrt{2} g_1 N_{i1} X_{m2} + y_\mu N_{i3} X_{m1}, \\ F_1^N(x) &= \frac{2}{(1-x)^4}\Big(1 - 6x + 3x^2 + 2x^3 - 6x^2 \ln(x)\Big), \\ F_2^N(x) &= \frac{3}{(1-x)^3}\Big(1 - x^2 + 2x \ln(x)\Big). \end{aligned} \tag{3.2}$$

The mass matrices N_{ij} and X_{mn} are defined in equations 2.4 and 2.7 respectively. The starred notation means taking the complex conjugate of that element. The Yukawa coupling is defined as:

$$y_\mu = \frac{g_2 m_\mu}{\sqrt{2} m_W \cos\beta}. \tag{3.3}$$

The g_1 is the $U(1)$ coupling and the g_2 is the $SU(2)$ coupling. All couplings are to be evaluated at the m_Z scale.

Applying the same procedure to the chargino diagram yields the following expression [37]:

$$\delta a_\mu^{\tilde{\chi}^\pm} = \frac{m_\mu}{16\pi^2}\sum_{k=1}^{2}\Bigg\{\frac{m_\mu}{12m^2_{\tilde{\nu}_\mu}}(\mid c_k^L \mid^2 + \mid c_k^R \mid^2)F_1^C\left(\frac{m^2_{\tilde{\chi}_k^\pm}}{m^2_{\tilde{\nu}_\mu}}\right) + \frac{2}{3}\frac{m_{\tilde{\chi}_k^\pm}}{m^2_{\tilde{\nu}_\mu}}\mathrm{Re}[c_k^L c_k^R]F_2^C\left(\frac{m^2_{\tilde{\chi}_k^\pm}}{m^2_{\tilde{\nu}_\mu}}\right)\Bigg\}. \tag{3.4}$$

The sum with index k runs over all chargino mass eigenstates. The sneutrino ($m_{\tilde{\nu}_\mu}$) has only one mass eigenstate, so no sum is required. The c_k terms and F_i^C functions are given by:

$$\begin{aligned} c_k^L &= -g_2 V_{k1}, \\ c_k^R &= y_\mu U_{k2}, \\ F_1^C(x) &= \frac{2}{(1-x)^4}\Big(2+3x-6x^2+x^3+6x\ln(x)\Big), \\ F_2^C(x) &= \frac{3}{2(1-x)^3}\Big(-3+4x-x^2-2\log(x)\Big). \end{aligned} \tag{3.5}$$

Again, V_{kl} and U_{kl} are defined as in equation 2.2.

From equations 3.1 and 3.4 we can deduce which pMSSM parameters will influence the anomalous magnetic moment. We can also estimate how large these contributions can become by taking into account the possible values for these parameters. From the mass matrices 2.2, 2.3 and 2.5 we see that the six parameters μ, $\tan\beta$, M_2, M_1 and the smuon masses ($M_{\tilde{e}}^R$ and $M_{\tilde{e}}^L$) directly contribute. From equations 3.1 and 3.4 we can estimate that we require a large value of $\tan\beta$ and small values for $M_{\tilde{e}}^R$ and $M_{\tilde{e}}^L$ to get a large contribution from the pMSSM.

3.2 Second-order diagrams

We will now examine second-order diagrams. First-order diagrams always had the lepton number carried by a supersymmetric particle. In second-order diagrams this is no longer a necessity, so we make a distinction between diagrams; either the lepton number is carried over by a SM particle or by a supersymmetric one. If carried over by a SM particle, it can cause new types of diagrams or change the existing Higgs-boson SM diagrams. Second-order diagrams where the lepton number is carried over by a supersymmetric particle are similar to the first-order pMSSM diagrams and therefore only add a small correction to these [38]. Let us first examine these.

Second-order corrections to first-order pMSSM diagrams ($\delta a_\mu^{\text{pMSSM, SO QED}}$)
One can either draw an extra vector boson line between the two muons in the first-order diagram, or one can draw an extra particle loop attached to any of the particle lines present in the diagrams in figure 3.1. An example diagram for a correction to the first-order chargino diagram is shown in figure 3.2. These types of diagrams usually have the same parameter dependence as the first-order diagrams. New parameters that contribute are suppressed due to the second-order nature at which they appear.

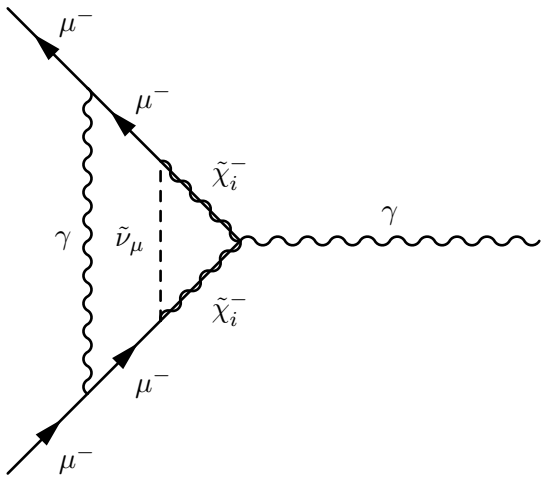

FIGURE 3.2: An example of a second-order diagram that causes a higher-order QED correction to a first-order chargino pMSSM diagram.

The total correction to the first-order pMSSM contributions can be decomposed, similar to equation 1.22, as

$$\delta a_\mu^{(a)} \approx c_L^{\text{pMSSM}} \log \frac{M_{SUSY}}{m_\mu} + c_0^{\text{pMSSM}}.$$

As is the case in the SM, the logarithmic term is argued to be dominant and has been calculated using effective field theory techniques, see [38]. The non-logarithmic term has not been calculated but is estimated to be negligible and thus we will assume $c_0^{\text{pMSSM}} = 0$. This gives rise to a correction factor to the first-order expressions:

$$\delta a_\mu^{\text{pMSSM, F.O. correction}} = (\delta a_\mu^{\tilde{\chi}^0} + \delta a_\mu^{\tilde{\chi}^\pm}) \Big(- \frac{4\alpha_{em}}{\pi} \log \frac{M_{\text{SUSY}}}{m_\mu} \Big). \tag{3.6}$$

Next to these corrections, there are also corrections where an EW vector boson is exchanged between the muons. Furthermore, there are new types of diagrams possible where the lepton number is carried by a supersymmetric particle. Both of these types of diagrams have not yet been evaluated and will therefore not be given here.

Second-order diagrams with the lepton number carried by an SM particle
We will now look at diagrams arising from the second-order pMSSM contributions that aren't corrections of first-order diagrams. Diagrams that fall into this category must have at least a muon or muon neutrino in one of the two loops. In particular, two-loop SM diagrams with a Higgs boson fall into this category, figure 3.3a. Another possibility is a SM one-loop diagram, where the vertex with the photon is enlarged into an extra loop. These diagrams are called Barr-Zee diagrams, an example can be found in figure 3.3b.

The two-loop SM diagrams with a Higgs boson will change the coefficients found in equation 1.22 to be [20]:

$$
\begin{aligned}
c_L^{\text{pMSSM}} &= \frac{1}{30}\{98 + 9c_L^h + 23(1 - 4\sin^2\theta_W)^2\}, \\
c_L^h &= \frac{M_Z^2 \cos 2\beta}{\cos\beta}\left[\frac{\cos(\alpha)\cos(\alpha+\beta)}{m_{H^0}^2} + \frac{\sin(\alpha)\sin(\alpha+\beta)}{m_{h^0}^2}\right].
\end{aligned} \tag{3.7}
$$

The term between brackets is equal to 1 at tree level, as this is exactly the mass relation in the Higgs sector in the pMSSM. This implies that the logarithms in both the SM and pMSSM are identical. The c_0 term in equation 1.22 is altered slightly by δc_0, but since it is negligibly small we will assume $\delta c_0 = 0$. As this term is the only way for the contribution of two-loop SM Higgs diagrams to change, we will not have to worry about them. Note however, if we accept a theory where one of the Higgs boson masses can be very small compared to the SM Higgs boson mass, the altered c_0 term could modify the contribution enough for it to matter.

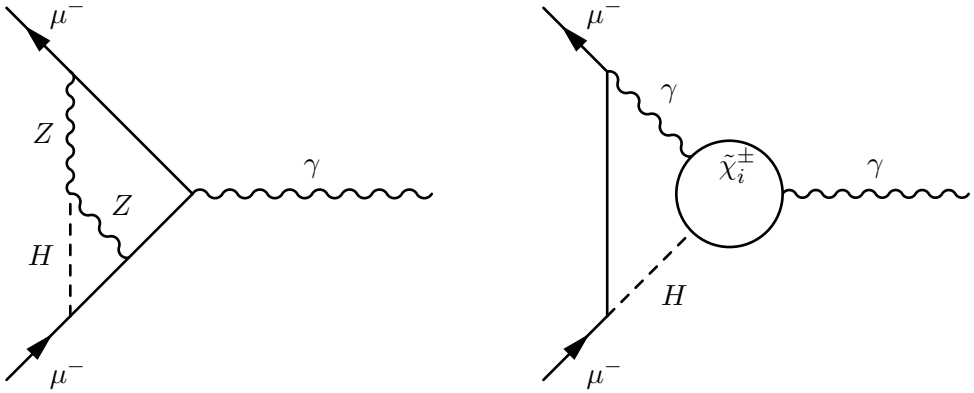

(A) A second-order SM diagram containing a Higgs boson. This Higgs boson could now be any neutral pMSSM Higgs boson.

(B) A photonic Barr-Zee diagram. The photon/Higgs boson in the loop can be replaced by other vector bosons.

FIGURE 3.3: Examples of second order diagrams appearing within the pMSSM calculations of the anomalous magnetic moment.

Let us now look at another possibility of a diagram where the lepton number is carried by a SM particle: a Barr-Zee diagram. An example is shown in figure 3.3b. The Barr-Zee contributions are especially relevant since the Higgs-sfermion coupling can become quite large in the pMSSM.

The specific diagram shown in figure 3.3b is the highest contributing second-order diagram. Other Barr-Zee diagrams, where the photon and Higgs boson in the first loop are exchanged with other vector bosons contribute similarly, but their contributions are smaller. An expression for the diagram in figure 3.3b has been found by first computing the effective vertex between the Higgs, photon and vector boson and only then computing the loop between them, see [39]. This is why this contribution has a similar structure to the expressions of the first order contributions. The

contribution, with a chargino loop is given by [40][41]:

$$\delta a_\mu^{\tilde{\chi}\gamma H} = \frac{\alpha_{em}^2 m_\mu^2}{8\pi^2 M_W^2 \sin^2\theta_W} \sum_{k=1}^{2} \Big[\mathrm{Re}[\lambda_\mu^{A^0} \lambda_{\tilde{\chi}_k^\pm}^{A^0}] F_{A^0}\left(\frac{m_{\tilde{\chi}_k^\pm}^2}{M_{A^0}^2}\right) + \sum_{l=\{h^0,H^0\}} \mathrm{Re}[\lambda_\mu^l \lambda_{\tilde{\chi}_k^\pm}^l] F_l\left(\frac{m_{\tilde{\chi}_k^\pm}^2}{M_l^2}\right) \Big]. \tag{3.8}$$

The diagram can also contain a sfermion instead of a chargino in the loop. The contribution for sfermions is given by [40][41]:

$$\delta a_\mu^{\tilde{f}\gamma H} = \frac{\alpha_{em}^2 m_\mu^2}{8\pi^2 M_W^2 \sin^2\theta_W} \sum_{\tilde{f}=\{\tilde{t},\tilde{b},\tilde{\tau}\}} \sum_{m=1}^{2} \Big[\sum_{l=\{h^0,H^0\}} (N_C Q^2)_{\tilde{f}} \mathrm{Re}[\lambda_\mu^l \lambda_{\tilde{f}_m}^l] F_{\tilde{f}}\left(\frac{m_{\tilde{f}_m}^2}{M_l^2}\right) \Big]. \tag{3.9}$$

The sums are again to incorporate every possible coupling; the k, m and i indices used in equations 3.8 and 3.9 are the same as in equation 3.1. However, m now sums over the mass eigenstates of the specific sfermion in question. The $\tilde{f}$ index gives the three possible third generation sfermions ($\tilde{f} = \{\tilde{t}, \tilde{b}, \tilde{\tau}\}$) and the l index denotes the light and heavy CP-even Higgs bosons ($l = \{h^0, H^0\}$). The N_C marks the colour degrees of freedom and Q is the charge of the sfermion in the loop divided by e. The 12 different λ couplings can be expressed as:

$$\lambda_\mu^{\{h^0,H^0,A^0\}} = \frac{\{-\sin\alpha, \cos\alpha, \sin\beta\}}{\cos\beta},$$

$$\lambda_{\tilde{\chi}_k^\pm}^{\{h^0,H^0,A^0\}} = \frac{\sqrt{2}M_W}{m_{\tilde{\chi}_k^\pm}} (U_{k1}V_{k2}\{\cos\alpha, \sin\alpha, -\cos\beta\} - U_{k2}V_{k1}\{\sin\alpha, -\cos\alpha, \sin\beta\}),$$

$$\lambda_{\tilde{f}_m=\{\tilde{t}_m,\tilde{b}_m,\tilde{\tau}_m\}}^{h^0} = \frac{2m_f}{m_{\tilde{f}_m}^2} \Big(\Big\{ \frac{A_t}{\sin\beta}, \frac{-\mu}{\cos\beta}, \frac{-\mu}{\cos\beta} \Big\} \cos\alpha + \Big\{ \frac{\mu}{\sin\beta}, \frac{-A_b}{\cos\beta}, \frac{-A_\tau}{\cos\beta} \Big\} \sin\alpha \Big) (U_{m1})^* U_{m2},$$

$$\lambda_{\tilde{f}_m=\{\tilde{t}_m,\tilde{b}_m,\tilde{\tau}_m\}}^{H^0} = \frac{2m_f}{m_{\tilde{f}_m}^2} \Big(\Big\{ \frac{A_t}{\sin\beta}, \frac{-\mu}{\cos\beta}, \frac{-\mu}{\cos\beta} \Big\} \sin\alpha - \Big\{ \frac{\mu}{\sin\beta}, \frac{-A_b}{\cos\beta}, \frac{-A_\tau}{\cos\beta} \Big\} \cos\alpha \Big) (U_{m1})^* U_{m2},$$

where in the last two couplings, the $m_{\tilde{f}_m}$ is the sfermion particle mass, m_f the corresponding SM particle mass and α the mixing angle between the CP-even Higgs bosons as defined in equation 2.1. The loop functions are given in appendix A.

The trilinear coupling A_f and Higgs mass parameter m_A directly influence the second order contribution. There are therefore 8 important parameters for the second-order contributions: μ, $\tan\beta$, M_1, M_2, m_A, and the three different trilinear couplings A_t, A_b and A_τ. When the smuon masses are large, the first order corrections will be suppressed. In that case, these second order Barr-Zee diagrams can play an important role.

Other second-order diagrams and higher
As already mentioned above, there are second-order diagrams which have not been evaluated yet. This means the true total second-order contribution can not be determined. However, estimates have been given for some of these diagrams and uncertainties have been proposed for neglecting others. We will briefly list them here.

We have omitted diagrams where a Z-or a W-boson is exchanged instead of the photon as in figure 3.2. The uncertainty caused by this omission has been estimated to be roughly $\pm 2 \cdot 10^{-10}$ by [42]. Subclasses of these diagrams have been evaluated since in [43] and fall within this uncertainty.

A similar uncertainty occurs by only evaluating Barr-Zee diagrams with a photon exchange. The uncertainty made due to not considering Z-and W-boson exchanges is estimated by [20] and [44] to be negligible in a large part of the pMSSM parameter space.

The total pMSSM contribution can be calculated by summing the first-order contribution, including the QED second-order corrections, given by equation 3.6 with the second-order Barr-Zee contributions given by equations 3.8 and 3.9:

$$\delta a_\mu^{\text{pMSSM}} = (\delta a_\mu^{\chi^0} + \delta a_\mu^{\chi^\pm})\Big(- \frac{4\alpha}{\pi} \log \frac{M_{\text{SUSY}}}{m_\mu}\Big) + \delta a_\mu^{\tilde{\chi}\gamma H} + \delta a_\mu^{\tilde{f}\gamma H}.$$

One has then neglected multiple second-order diagrams and higher-order diagrams. The uncertainty estimates for the second-order diagrams has been given above. The uncertainty caused by not including higher-order diagrams has been estimated by [40] to be roughly $\pm 1.5 \cdot 10^{-10}$. Furthermore, [40] suggests adding these uncertainties linearly to get a total uncertainty estimate of

$$\delta a_\mu^{\text{pMSSM, uncertainty}} \approx \pm \Big[0.025 \cdot \delta a_\mu^{\text{pMSSM}} + 3.5 \cdot 10^{-10} \Big]. \tag{3.10}$$

Chapter 4

Computational programs and results

As illustrated in the previous two chapters, calculating the pMSSM contribution to the anomalous magnetic moment is not easily done. Many of the variables in the analytic expressions depend on the choice of the 19 free pMSSM parameters. These will determine all couplings, all supersymmetric particle masses and observables, combining into a full supersymmetry spectrum. To determine which pMSSM spectra can explain certain phenomena, one has to start with picking values for the 19 input parameters. From that one can determine the corresponding spectrum and then one can calculate all the diagrams required for the specific phenomenon. Here, we look at the anomalous magnetic moment, where one needs all 19 parameters to generate the spectrum, followed by calculating the largest contributions sketched in chapter 3.

There are several software programs written to calculate the supersymmetric spectrum and observables like the anomalous magnetic moment. If one finds a suitable value for the anomalous magnetic moment, the spectrum still needs to conform to certain boundary conditions. If one generates a spectrum without a Higgs boson at a mass of roughly 125 GeV, one can disregard the spectrum. Another constraint that is usually implemented, is the dark matter constraint, where one assumes the lightest supersymmetric particle to have no electric charge.

The software programs mentioned above are used by many theoretical physicists and can be divided into two categories. The first category of programs is called a spectrum generator. It requires a number of input parameters and uses those to calculate a full supersymmetric spectrum. In the case of the pMSSM, these input parameters are the 19 discussed in chapter 2.3. The resulting spectrum can then be used to calculate observables of interest. The other type of program requires a full spectrum as input. These programs are usually more specialised in calculating specific observables.

In this thesis we will be comparing two software programs, each specialised in different observables. The programs are called SuperISO [45] and MicrOMEGAs [46]. They both require a spectrum as input. We will use the spectrum generator SPheno [47] to provide this spectrum.

In 2003, the SUSY Les Houches accord (SLHA) was established [48]. This streamlined the way all these software programs handle input and provide output, and made sure every program uses the same conventions. The input for and output of

such programs are stored in a SLHA file. The three programs we use in this thesis all use SLHA files for input and output.

4.1 SPheno

SPheno is short for Supersymmetric Phenomenology. As mentioned, it is a spectrum generator, written in Fortran. Besides generating a full supersymmetric spectrum, it also calculates decay widths, cross sections (for e^+e^- colliders) and branching ratios of supersymmetric particles and Higgs bosons. It can also calculate specific processes, like $b \to s\gamma$ and the anomalous magnetic moment of both the muon and electron [47].

To generate a spectrum, SPheno calculates the renormalisation group equations (RGEs) up to second-order. For the evaluation of the decay widths and cross sections, the higher-order effects are only incorporated in the couplings. SPheno calculates most quantities at tree level, but uses these couplings with higher-order contributions in them. It also does this for the anomalous magnetic moment. In the code of SPheno, four contributions to the anomalous magnetic moment are calculated, labeled as a_μ^{11}, a_μ^{12}, a_μ^{21} and a_μ^{22}. They are given by:

$$\begin{aligned}
a_\mu^{11} &= \frac{m_\mu \alpha_{em}}{4\pi \sin^2\theta_W} \sum_{j=1}^{4}\sum_{k=1}^{2} \frac{1}{M_{\tilde{\chi}_j^0}} \eta_{\mu j}^k F_1\left(\frac{M^2_{\tilde{\mu}_k}}{M^2_{\tilde{\chi}_j^0}}\right), \\
a_\mu^{12} &= \frac{m_\mu^2 \alpha_{em}}{24\pi \sin^2\theta_W} \sum_{j=1}^{4}\sum_{k=1}^{2} \frac{1}{M^2_{\tilde{\chi}_j^0}} X_{\mu j}^k F_2\left(\frac{M^2_{\tilde{\mu}_k}}{M^2_{\tilde{\chi}_j^0}}\right), \\
a_\mu^{21} &= \frac{m_\mu \alpha_{em}}{4\pi \sin^2\theta_W} \frac{m_\mu}{\sqrt{2} m_W \cos\beta} \sum_{i=1}^{2} \frac{1}{M_{\tilde{\chi}_i^+}} Re(U_{i2}^* V_{i1}^*) F_3\left(\frac{M^2_{\tilde{\nu}}}{M^2_{\tilde{\chi}_i^+}}\right), \\
a_\mu^{22} &= \frac{m_\mu^2 \alpha_{em}}{24\pi \sin^2\theta_W} \sum_{i=1}^{2} \frac{1}{M^2_{\tilde{\chi}_i^+}} \left(\frac{m_\mu^2}{2m_W^2 \cos^2\beta} |U_{i2}|^2 + |V_{i1}|^2\right) F_4\left(\frac{M^2_{\tilde{\nu}}}{M^2_{\tilde{\chi}_i^+}}\right).
\end{aligned} \tag{4.1}$$

These expressions are based on the calculations in [49] and [50]. The parameters in these equations are all running paramaters. We identify these first two expressions as being the first-order neutralino contributions and the last two expressions as the chargino contributions. They are similar to equations 3.1 and 3.4, but written somewhat differently. The benefit of this notation is that it is easy to identify one order of α_{em} and the m_μ dependence. However, the neutralino couplings $\eta_{\mu j}^k$ and $X_{\mu j}^k$ become more complicated. Exact expressions for these and the loop functions F_1 - F_4, and the equivalence between equations 4.1 and 3.1 and 3.4 can be found in appendix A.

It is important to note that SPheno only calculates the contributions in equations 4.1. These contributions include higher-order corrections to the couplings, but exclude the higher-order contributions coming from different types of diagrams, as those shown in chapter 3. As SPheno uses higher-order couplings, it is outside the scope of this thesis to identify the origin of the differences between Spheno and the other two programs. Hence, we focus on the differences between MicrOMEGAs and SuperISO, which are widely used by the scientific community.

4.2 MicrOMEGAs and SuperISO

Both MicrOMEGAs and SuperISO require a spectrum as input, which we provide using SPheno. Both programs are compatible with other spectrum generators as well. Both programs calculate the first-order contribution as given in equations 3.1 and 3.4 but will overestimate the first-order pMSSM contribution to δa_μ as mentioned in chapter 3.2. This is because they cannot generate their own spectrum and as such, do not use running couplings. We have given an expression to correct for this in equation 3.6. Only SuperISO implements this correction. Besides that, only SuperISO implements the higher-order contributions from the Barr-Zee diagrams.

4.2.1 MicrOMEGAs

MicrOMEGAs is a program designed to perform (cold) dark matter studies. To be more precise, it calculates the dark matter relic density, certain cross sections between dark matter particles and nuclei relevant for direct detection and spectra of particles that would be created in astrophysical dark-matter annihilation processes (like e^+ and γ) [46]. It supports many different SM extensions, including the (p)MSSM. It is written in both C and Fortran and has a module for calculating the anomalous magnetic moment called 'gmuon()'.

The module 'gmuon()' calls for a set of input parameters. These are listed in table 4.1. The last four entries in this table are actually not used in the module, but we include them here for completeness.

Variable	Value	Origin
m_μ	0.1057	Hardcoded
m_Z	91.1876	Hardcoded
m_W	79.958	Calculated from m_Z and $\cos\theta_w$
$\sin\theta_w$	0.48076	Hardcoded
α_{em}	$7.81653 \cdot 10^{-3}$	Hardcoded
mod(M_1) & arg(M_1)		Taken from spectrum file
mod(M_2) & arg(M_2)		Taken from spectrum file
mod(μ) & arg(μ)		Taken from spectrum file
mod(A_μ) & arg(A_μ)		Taken from spectrum file

TABLE 4.1: MicrOMEGAs input parameters.

Note that the value for α_{em} is given at a specific scale, above the electroweak scale.

Besides the input parameters given in the first five entries of the above table, MicrOMEGAs calls for all other needed parameters while executing the module. Parameters included in this are M_1 and M_2, hence mod(M_1) and such are not needed. Most of these are taken from the spectrum file from SPheno. However, some are hardcoded instead. We will elaborate further on this in chapter 4.4.

The matrices N, U and V that diagonalise the mixing matrices are all taken from the spectrum file, as well as all the mass eigenstates of the neutralinos, charginos and the muon sneutrino. The smuon mass eigenstates are calculated by diagonalising

the smuon mixing matrix (equation 2.8). The values for $M^L_{\tilde{e}}$, $M^R_{\tilde{e}}$, μ and $\tan\beta$ are taken from the spectrum file and A_μ is set to 0. Note that $\tan\beta$ is actually set to the input value, not to the running value at the m_Z scale, even though both are available in the spectrum file. Finally, the smuon mixing matrix itself is determined by using equation 2.7.

The $U(1)_Y$, $SU(2)_L$ and Yukawa couplings are calculated, even though they are also available to read in from the spectrum file. They are determined by:

$$g_1 = \frac{\sqrt{4\pi\alpha_{em}}}{\cos\theta_w}, \qquad g_2 = \frac{\sqrt{4\pi\alpha_{em}}}{\sin\theta_w}, \qquad y_\mu = \frac{m_\mu g}{\sqrt{2}M_W\cos\beta}.$$

This means they are determined from hardcoded values and will differ slightly compared to the spectrum file that SPheno provides for a given set of inputs.

These are all the parameters that are needed for the calculation. MicrOMEGAs splits the calculation into a for-loop for the neutralino part and a for-loop for the chargino part, for which it uses exactly the expressions of equations 3.1 and 3.4. It sums up all these contributions into a single variable called `g_muo`. The other contributions discussed in chapter 3 are not computed, hence the total contribution calculated by MicrOMEGAs is only a first-order one.

4.2.2 SuperISO

SuperISO is a tool written in C and is designed for flavour-physics calculations. The main goal of the program was to calculate the process $B \to K^*\gamma$, but many other flavour decays and branching ratios have been added, as well as the anomalous magnetic moment [45]. It needs a spectrum as input, just as MicrOMEGAs. SuperISO supports various supersymmetry scenarios and has also included the general two-Higgs-doublet model (2HDM).

SuperISO also suggests a limit for the anomalous magnetic moment, which can be used to disregard certain supersymmetric spectra as feasible. This limit is suggested as: $-2.4\cdot10^{-10} < a_\mu < 5.0\cdot10^{-9}$ [45].

The module 'gmuon.c' is responsible for the calculation of the anomalous magnetic moment. Before the program calls this module, a specific model has to be chosen. If no model is chosen it defaults to the general MSSM model, which is equivalent to the model that the calculations of SPheno and MicrOMEGAs use. This module then requires input parameters to be provided, which can be found in table 4.2.
Besides the input parameters, the module calls for other parameters required for the calculation during its execution. Most of these parameters are taken from the spectrum file provided by SPheno. Exceptions are the Yukawa coupling, which is calculated in the same way as done by MicrOMEGAs, and $\sin\theta_w$ which is calculated by $\sin(\arctan(g_1/g_2))$. The smuon mass eigenstates and mixing matrix are determined in the same way as done by MicrOMEGAs.

In constrast to MicrOMEGAs, SuperISO does take the couplings g_2 and g_1 from the spectrum file, where they are given at the m_Z scale. The running value of $\tan\beta$ is taken from the spectrum file instead of the input value. SuperISO calls for more parameters than the other two programs, as it also calculates the Higgs corrections

Variable	Value	Origin
m_μ	0.105658372	Taken from spectrum file
m_Z	91.1876	Hardcoded
m_W	80.3184459	Taken from spectrum file
$\sin\theta_w$	0.4807913151	Calculated from g_1 and g_2
α_{em}	$7.866706525 \cdot 10^{-3}$	Taken from spectrum file
mod(A_μ) & arg(A_μ)	0	Taken from spectrum file

TABLE 4.2: SuperISO's exact input parameters.

to SM diagrams and the photonic Barr-Zee contributions (equations 3.8 and 3.9). The first-order calculation done by SuperISO is determined by:

$$\delta a_\mu^{f.o.} = \delta a_\mu^{\tilde{\chi}^0} + \delta a_\mu^{\tilde{\chi}^\pm} + \delta a_\mu^{H^0} + \delta a_\mu^{A^0} + \delta a_\mu^{h^0} + \delta a_\mu^{H^\pm}$$

The first two terms are identical to equations 3.1 and 3.4. The last four terms are corrections to the 1-loop SM diagram containing a Higgs Boson. They are heavily suppressed in the SM and even more so in the MSSM. The reason they are calculated by SuperISO is due to the fact that no specific model was chosen. In the next-to-minimal supersymmetric standard model (NMSSM) or 2HDM these terms can contribute. For exact expressions of these contributions, see [45]. In the MSSM, these terms are usually smaller than 10^{-15} and will therefore be neglected here.

The first-order calculation is corrected by a factor of $(1 - \frac{4\alpha_{em}}{\pi} \ln \frac{M_{\text{SUSY}}}{m_\mu})$ to account for higher-order corrections, see equation 3.6. Furthermore, SuperISO also calculates the second-order (bosonic) electroweak corrections to SM diagrams due to the extra pMSSM Higgs Bosons, as shown in equations 1.22 and 3.7. The δc_0 influence to c_0 in equation 1.22 is set to 0 and c_L^h in equation 3.7 is set to 1 by SuperISO when choosing no model, see [49]. This means that the second-order electroweak contributions to a_μ are similar in the pMSSM as they are in the SM, the important effects are incorporated in the running term of equation 3.6. For other models, these diagrams with Higgs bosons can change the SM contribution to δa_μ substantially, which explains why SuperISO calculates them.

Finally, SuperISO also calculates the Barr-Zee diagrams given in figure 3.3b, which do contribute in the pMSSM. We would like to point out however, that the loop functions SuperISO uses in the second-order calculations are based on an approximation of the analytical function given in equation b.1. This approximation is very good for most of the range of the mass ratio x, except around $x \approx 100$. The approximation is given in appendix A and the differences between the approximation and analytical function can be seen in figure C.8 in appendix B. The total pMSSM contribution calculated by SuperISO can thus be written as:

$$\delta a_\mu^{\text{MSSM}} = \left(\delta a_\mu^{\tilde{\chi}^0} + \delta a_\mu^{\tilde{\chi}^\pm}\right)\left(1 - \frac{4\alpha_{em}}{\pi} \ln \frac{M_{\text{SUSY}}}{m_\mu}\right) + \delta a_\mu^{\tilde{\chi}\gamma H} + \delta a_\mu^{\tilde{f}\gamma H}.$$

Note that M_{SUSY} is given by the spectrum file.

4.3 The six important first-order parameter dependencies

Let us first take a look at the parameter dependence of δa_μ for the programs. As explained in chapter 3.1, the main parameters that play a role in the first-order pMSSM contributions are M_1, M_2, μ, $M_{\tilde{e}}^L$, $M_{\tilde{e}}^R$ and $\tan\beta$. To get a qualitative look at these parameters, we tune most of the other parameters in such a way that their effects become negligible. For example, if we want the Higgs sector to interfere as little as possible, we can tune m_A very high, such that contributions from the Higgs bosons become very small. Similarly, tuning the sfermion mass parameters, other than $M_{\tilde{e}}^L$ and $M_{\tilde{e}}^R$, very high will reduce their involvement via RGEs as well.

A random scan was programmed such that M_1, M_2, μ, $\tan\beta$, $M_{\tilde{e}}^L$ and $M_{\tilde{e}}^R$ could be varied over a wide range. The other parameters were chosen to only vary slightly around 4 TeV. The range for M_1, M_2, μ, $M_{\tilde{e}}^L$ and $M_{\tilde{e}}^R$ was set between 40 GeV and 4 TeV, while $\tan\beta$ could vary from 2 to 58. First, a random scan sampling 25000 points with these values for the parameters was performed. From these parameter sets, one with a contribution close to the SM value for δa_μ was chosen to perform targeted scans, where the important parameters were varied one by one while keeping all other parameters static. Note that this spectrum has no specific significance other than being a bench mark for the targeted scans. From these tests, we will get a qualitative insight in how δa_μ responds to the important parameters. The table below shows the static values of the important parameters.

$\tan\beta$	$M_{\tilde{e}}^L$	$M_{\tilde{e}}^R$	M_1	M_2	μ
50.78	566.5	463.5	620.4	966.8	3456

TABLE 4.3: The parameter set used for the first-order parameter dependence of δa_μ. All mass parameters are given in GeV.

It is important to note that the second-order calculations performed by SuperISO were disabled during these tests, such that we get a clear picture of the first-order contributions. Besides that, no other constraints were implemented, but the constraints applied by SPheno are still in effect. This includes not allowing tachyonic particles to arise in the spectrum for example, see [47] for the specific constraints.

For some parameter dependencies, we will split up the total neutralino contribution into four separate contributions; one for each neutralino. We will then split those contributions up into two; one for each smuon. The reason for the split in smuons, is that their contributions due to the couplings solely depend on the values for X_{11} and X_{12} as determined by equation 2.7. Even though these are a function of multiple parameters, X_{11} is the cosine of a function of these parameters while X_{12} is the sine of that same function. If $X_{11} \approx 0$, then $X_{12} \approx \pm 1$ and $X_{21} \approx \mp 1$. In that case, we see from equation 3.2 that the squared couplings contribute with equal sign, but the product of left-handed and right-handed coupling differ in sign for the smuons. If we take $X_{11} \approx X_{12}$, we see a similar effect. This relative minus sign between the product of left-handed and right-handed couplings of the two smuon contributions has a greater effect for higher X_{12} values and will only vanish at $X_{12} = 0$, i.e. when there is no mixing between the sleptons. Note that the product of the couplings will contribute more due to it scaling with the neutralino mass, whereas the squared couplings scale with the (much smaller) muon mass.

When we show the individual contributions for the neutralinos, they will be for the lightest smuon unless there is a significant difference between the smuon contributions.

$\tan\beta$
The result for the variation in $\tan\beta$ can be seen in figure 4.1.

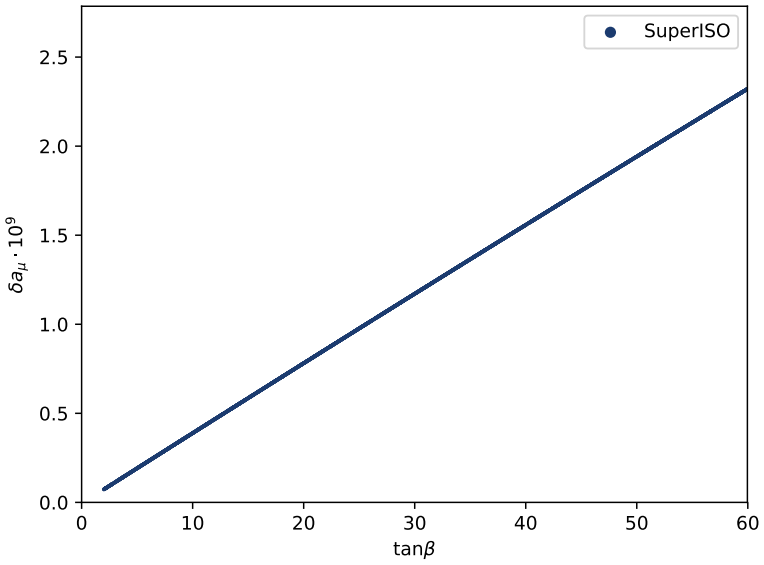

FIGURE 4.1: The δa_μ dependence on the parameter $\tan\beta$.

To understand the linear behaviour of $\tan\beta$, we can take a look at equations 3.2 and 3.5. The couplings n^L_{im} and n^R_{im} appear in the first-order neutralino contribution as either a product, or sum of squares. This means we get terms without a factor, with a single factor and with a squared factor of the Yukawa coupling, see appendix A for more detail. Remember, the Yukawa coupling as defined in equation 3.3 scales with $1/\cos\beta$.

Any term with no factor of the Yukawa coupling will stay constant while varying $\tan\beta$. Terms with a squared factor of the Yukawa coupling are heavily suppressed because the Yukawa coupling is of order m_μ/m_W. These terms will thus not play a significant role in the dependence of δa_μ on $\tan\beta$. The only terms that remain are the ones with a single factor of the Yukawa coupling. The Yukawa coupling scales linearly with $\tan\beta$ as long as $\tan\beta$ is sufficiently large (≥ 5) because $y_\mu \propto 1/\cos\beta \approx \tan\beta$.

$M^L_{\tilde{e}}$ and $M^R_{\tilde{e}}$
The dependence of δa_μ on $M^R_{\tilde{e}}$ is depicted in figure 4.2. The decrease of δa_μ can be explained by looking at the neutralino contributions in equation 3.1. We see an overall factor of $m^{-2}_{\tilde{\mu}}$, which is exactly the behaviour we see in figure 4.2. The loop functions could be able to alter this behaviour, but they will remain relatively constant when varying $M^R_{\tilde{e}}$ from 0 to 4 TeV. This is because when varying $M^R_{\tilde{e}}$, the mass ratio $x = m_{\tilde{\chi}^0_i}/m_{\tilde{\mu}_k}$ decreases from 25 down to 0.2, depending on which smuon

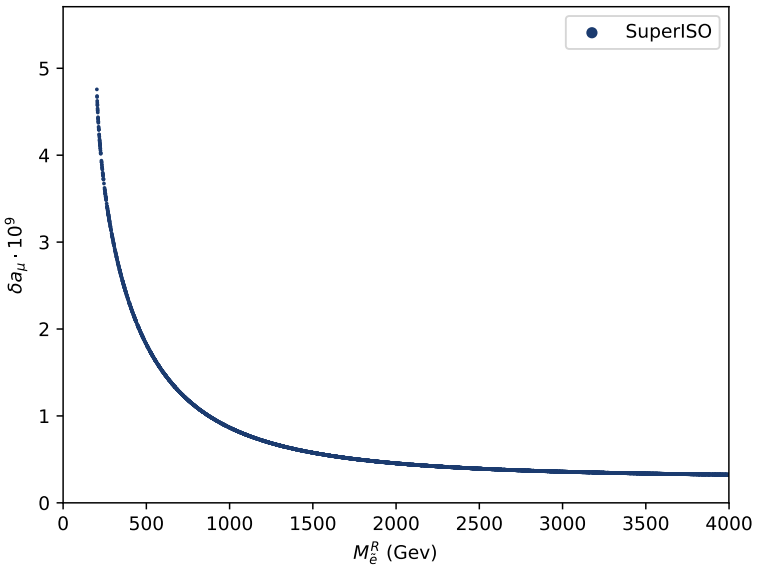

FIGURE 4.2: The δa_μ dependence on the parameter $M_{\tilde{e}}^R$.

and which neutralino one is evaluating. In figures C.1 and C.2 one can see that the change in value of the loop functions between $x = 25$ and $x = 0.2$ is small.

The chargino contribution scales with $m_{\tilde{\nu}_\mu}^{-2}$. When varying $M_{\tilde{e}}^R$, the mass of the muon sneutrino remains relatively constant running from $m_{\tilde{\nu}_\mu} \approx 580$ GeV down to $m_{\tilde{\nu}_\mu} \approx 540$ GeV. Note that this is of the same order as $M_{\tilde{e}}^L$, which is to be expected, as $\tilde{\nu}_\mu$ is a left-handed sparticle. Hence, the chargino contribution is also approximately constant. We see this in the tail end of figure 4.2, where the contribution to δa_μ is nonzero.

We have checked the results for $M_{\tilde{e}}^L$ as well, where we see similar characteristics, except that the contribution to δa_μ does become zero at high values of $M_{\tilde{e}}^L$. This can be explained by the fact that $m_{\tilde{\nu}_\mu}$ will again be of similar order in value as $M_{\tilde{e}}^L$ is. This means $m_{\tilde{\nu}_\mu} \approx 4$ TeV at the tail end of the variation in $M_{\tilde{e}}^L$. Hence the $m_{\tilde{\nu}_\mu}^{-2}$ factor causes the chargino contribution to become negligible.

M_1

The dependence on M_1 is shown by figure 4.3.
The peak around a value of $M_1 = 350$ GeV can be explained by examining the matrix elements and loop functions found in equation 3.2, as M_1 mostly influences the neutralino sector.

Let us first examine the loop functions naively: We assume for the couplings $n_{im}^L = n_{im}^R = 1$ and then see what behaviour we get from the loop functions and mass parameters in equation 3.1. The loop functions contributing to the neutralino contribution are F_1^N and F_2^N, for which the mass ratio dependence can be seen in figures C.1 and C.2 in appendix B. Here, we plot the neutralino contribution as a function of M_1 with the couplings set to one, so the effect of the loop functions can be seen as a function of M_1. This is shown in figure 4.4.

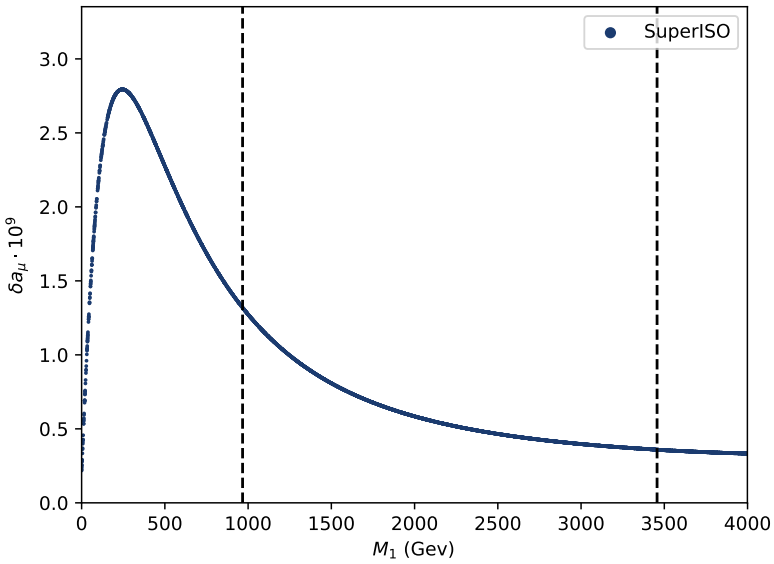

FIGURE 4.3: The δa_μ dependence on the parameter M_1. The first dashed line is at $M_2 = 966.8$ GeV and the second at $\mu = 3456$ GeV.

The peak of the plot is dominated by the $m_{\tilde{\chi}_i^0}$ factor in front of F_2^N. It already shows a somewhat similar shape as the actual results by SuperISO. Note that the argument of the loop function is the mass ratio with the mass of the neutralino in the numerator. Hence, when the mass of the neutralino increases, the ratio inside the loop function increases as well. Overall, the mass of the dominant neutralino increases as M_1 increases. To see this, we take a look at how and when M_1 influences the four neutralino masses.

We divide the figure into three different regions: $|M_1| < |M_2|$, $|M_2| < |M_1| < |\mu|$ and $|\mu| < |M_1|$. The first region, $|M_1| < |M_2|$, is where the lightest neutralino $\tilde{\chi}_1^0$ is Bino-dominated. This is because M_1 influences the Bino neutralino as can be seen in equations 2.3 and 2.4. The other neutralinos remain approximately constant in this region. When $|M_1|$ becomes larger than $|M_2|$, the Bino-dominated neutralino becomes heavier than the Wino-dominated neutralino. Because we order the neutralinos according to mass, we now have $\tilde{\chi}_2^0$ being the Bino-dominated neutralino. The Wino-dominated neutralino becomes the lightest neutralino, $\tilde{\chi}_1^0$, and remains constant while varying M_1 further. A similar change in ordering happens when $|M_1|$ becomes larger than $|\mu|$. Here, the Bino dominated neutralino becomes heavier than the Higgsino dominated neutralino. As such, the Bino dominated neutralino becomes $\tilde{\chi}_4^0$ and the Higgsino dominated neutralinos become $\tilde{\chi}_2^0$ and $\tilde{\chi}_3^0$.

When we plot the product of the couplings and the loop function for each neutralino individually, we expect to see a big change in contribution at the edges of these regions (i.e. around 966 and 3456 GeV). The loop functions for the three non-dominant neutralinos per region are approximately constant.

As SuperISO does not output the individual neutralino contributions, we calculate these ourselves using the output of SPheno. SPheno does not calculate the mixing matrix for the mixing between left-and right-handed sleptons but we retrieved those

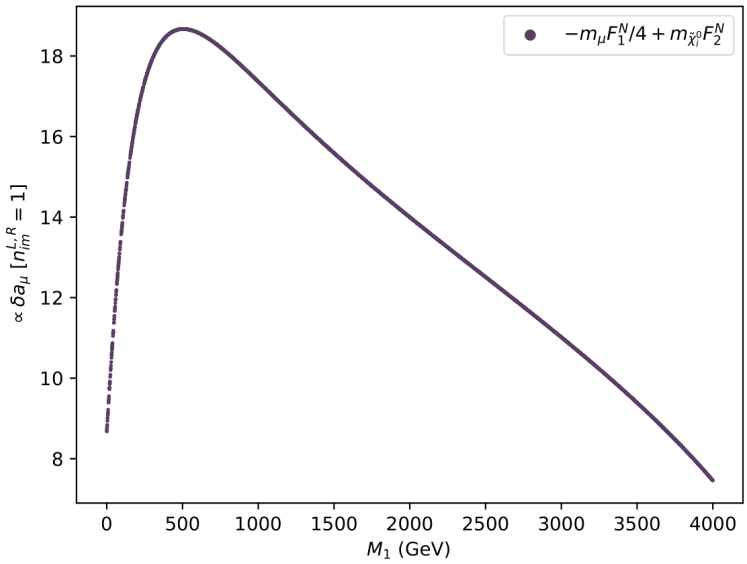

FIGURE 4.4: The result of $-m_\mu F_1^N/4 + m_{\tilde{\chi}_i^0} F_2^N$ for all four neutralinos combined.

by making use of equation 2.7.

The results for the first, second and fourth neutralino can be seen in figure 4.5, where we look only at $m_{\tilde{\mu}_1}$. The third neutralino has not been shown here, because its contribution is negligible over the entire range of M_1. This is because there is always a nearly pure Higgsino state neutralino. This is a combination of $\tilde{H}_u$ and $\tilde{H}_d$ but

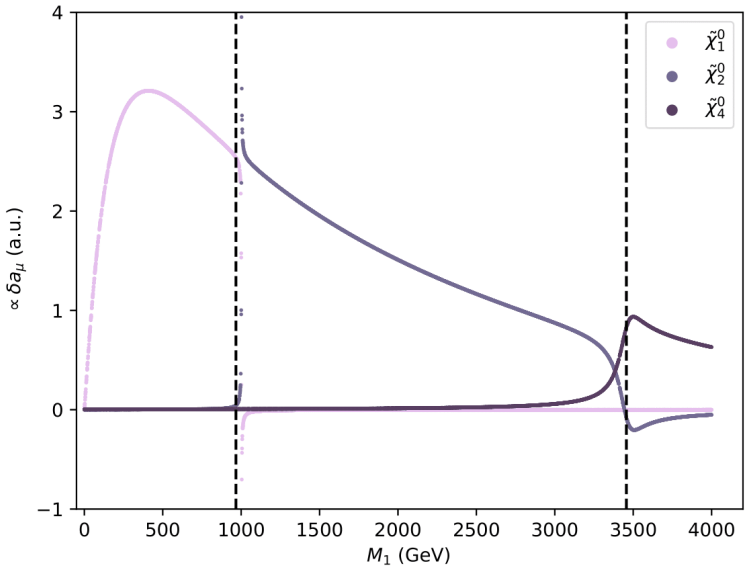

FIGURE 4.5: The behaviour of the first, second and fourth neutralino contributions for $m_{\tilde{\mu}_1}$ when varying M_1. The dashed lines indicate the values for which $|M_1|$ crosses $M_2 = 966$ GeV and $\mu = 3456$ GeV.

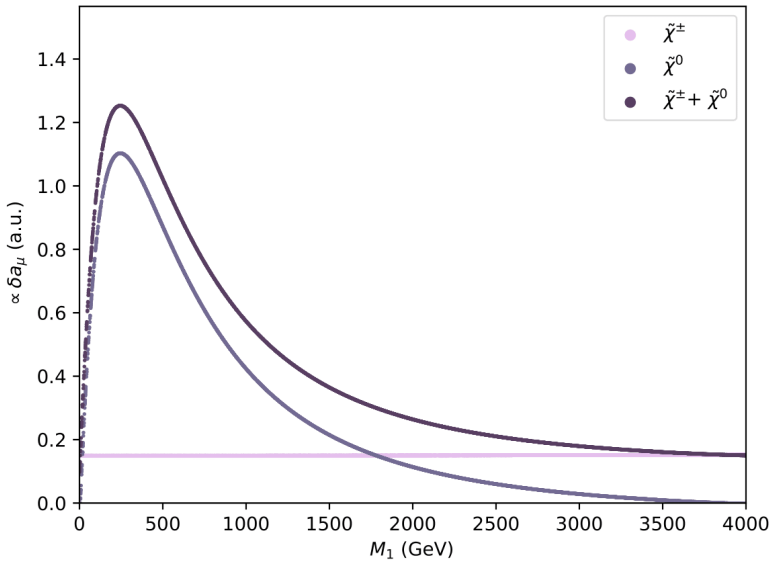

FIGURE 4.6: Chargino ($\tilde{\chi}^{\pm}$), Neutralino ($\tilde{\chi}^{0}$) and total ($\tilde{\chi}^{\pm} + \tilde{\chi}^{0}$) contribution for the M_1 parameter dependence.

hardly mixes with the Bino and Wino states. In this case, $\tilde{\chi}_3^0$ is nearly purely Higgsino, but $\tilde{\chi}_4^0$ is mostly Higgsino with some Bino and Wino mixing in there. For the other smuon, $m_{\tilde{\mu}_2}$, we see a similar behaviour but it is smaller in size and negative. The relative minus sign between the smuon contributions is explained at the start of chapter 4.3 and the reason the $m_{\tilde{\mu}_2}$ contribution is smaller is because $m_{\tilde{\mu}_2}$ is heavier. The behaviour of the individual neutralinos is also similar. This is due to the fact that μ is relatively large here, allowing mixing between the left-and right-handed states of the smuon.

We see that the contributions from the individual neutralinos change roughly at the borders where M_1 crosses M_2 and μ. This is due to the change in neutralino composition as discussed above.

Ultimately, the total neutralino contribution is a smooth curve as can be seen in figure 4.6. We also show the chargino contribution in this figure. It is constant while varying M_1, as expected, since M_1 does not influence the chargino mass. Combining both contributions perfectly recreates the peak and characteristics as seen from the output of SuperISO in figure 4.3. We conclude that for this parameter set the dependence is dominated by the behaviour of the loop functions and smoothed out by the couplings.

M_2

The dependence of δa_μ on M_2 is shown in figure 4.7. We now need to look at both the neutralino and chargino equations 3.1 and 3.4. Similarly to M_1, the individual neutralinos and charginos only contribute in specific regions, but the sum of their contributions is a smooth function of M_2. We show the neutralino and chargino contribution separately in figure 4.8.

Let us first focus on the chargino contribution. We see from figure 4.8 that there is

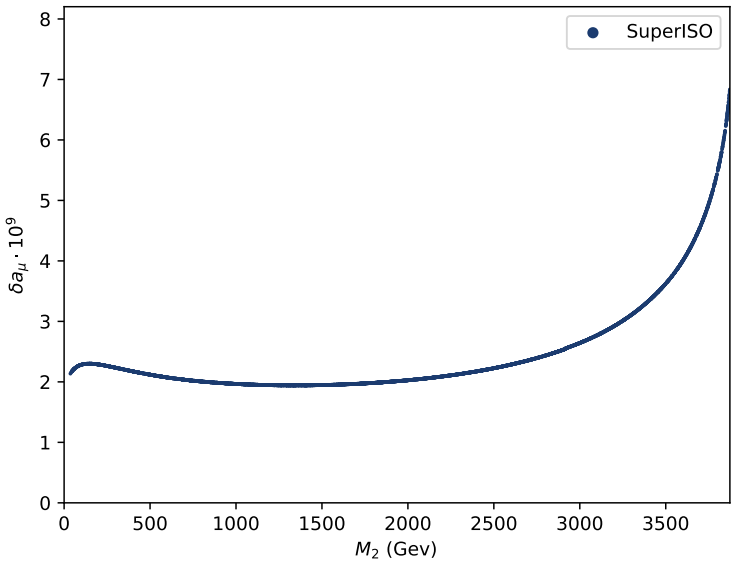

FIGURE 4.7: The δa_μ dependence on the parameter M_2.

a small bump around $M_2 = 200$ GeV. It is caused in a similar way as the peak in M_1; the loop function F_2^C is very large for low values of M_2 and decreases rapidly when M_2 rises. The chargino mass factor in front of the loop function increases as M_2 increases. Their product generates a peak at roughly $M_2 = 200$ GeV. The heavy chargino does not mirror this behaviour, as both the loop function and the mass factor are approximately constant at low values of M_2.

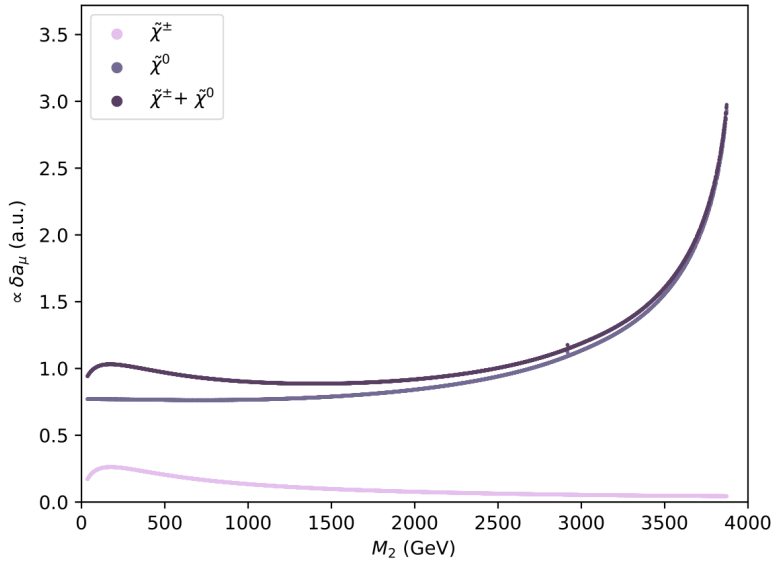

FIGURE 4.8: Chargino ($\tilde{\chi}^{\pm}$), Neutralino ($\tilde{\chi}^0$) and total ($\tilde{\chi}^{\pm} + \tilde{\chi}^0$) contribution for the M_2 parameter dependence.

The neutralino contribution is again the dominant contribution. We see a large increase in contribution for high values of M_2. However, we have checked that this is not due to the individual neutralino contributions; they remain relatively constant over the entire range of M_2.

The reason for the neutralino contribution blowing up at higher values of M_2 is due to the pre-factor of $m^{-2}_{\tilde{\mu}_{1,2}}$ in equation 3.1. The smuon masses both decrease at higher values of M_2. From the equations in chapter 2.1, we see no direct influence of M_2 on the smuon masses. However, the RGEs for the first family sleptons are influenced by M_2. One of the terms in the RGE for $M^L_{\tilde{e}}$ is $-3\mathcal{C}_2 g_2^2 M_2^2$, where $\mathcal{C}_2$ is the Casimir invariant for the Winos and g_2 the corresponding coupling, both positive. Hence, an increasing M_2 would decrease the running value of $M^L_{\tilde{e}}$ and thus reduce the mass of the smuons. With a decreasing smuon mass, the corresponding $m^{-2}_{\tilde{\mu}_{1,2}}$ rapidly increases which explains what we see in figure 4.8.

μ

The dependence of δa_μ on μ is shown in figure 4.9. As was the case with M_2, both the neutralino and chargino contributions are relevant for μ. We see a similar behaviour in figure 4.9 as we did for the M_2 variation; there is a local maximum at low values of μ and a rising contribution at higher values of μ. We have split up the neutralino and chargino contributions and plotted them in figure 4.10.

The peak at low values of μ can be explained in a similar way as was the case for M_2. This is caused by the chargino contribution, more specifically by the mass of the lightest chargino increasing in value while the loop function F_2^C is rapidly decreasing in that domain. The peak seems much larger than was the case for M_2, but that is because the neutralino contribution doesn't increase as rapidly at high values of μ.

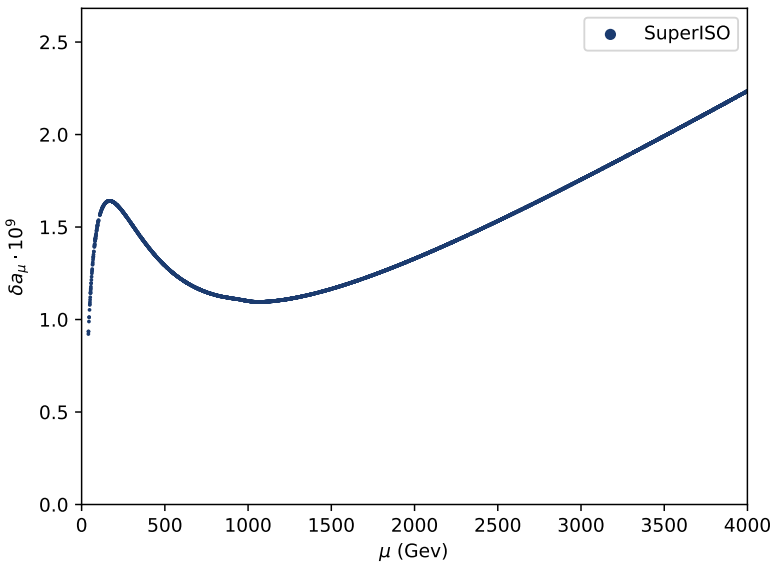

FIGURE 4.9: The δa_μ dependence on the parameter μ.

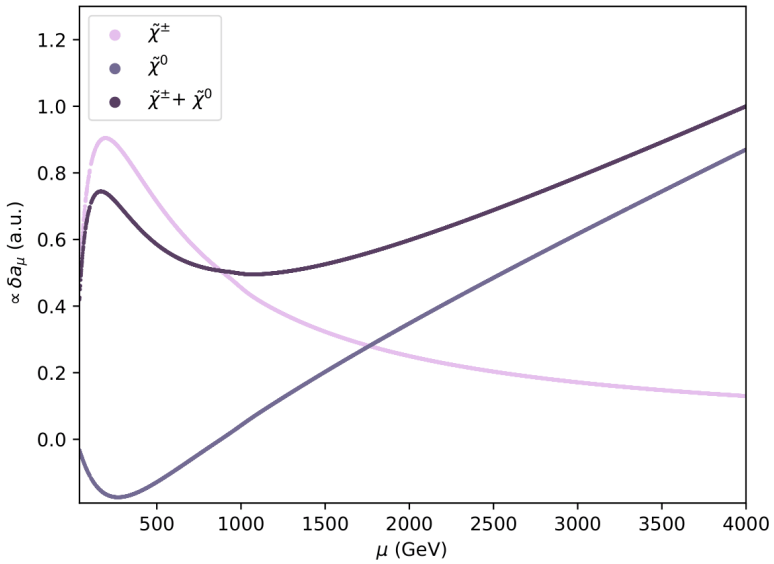

FIGURE 4.10: Chargino ($\tilde{\chi}^{\pm}$), Neutralino ($\tilde{\chi}^{0}$) and total ($\tilde{\chi}^{\pm}+\tilde{\chi}^{0}$) contribution for the μ parameter dependence.

Since μ only influences the mixing of the smuon mass parameters and does not influence the RGEs of $M_{\tilde{e}}^{L}$ or $M_{\tilde{e}}^{R}$, the masses of the smuons remain approximately constant over the entire variation of μ. This means the factor of $m_{\tilde{\mu}_{1,2}}^{-2}$ plays no role here. The linear increase of the neutralino contribution is caused by something else.

The neutralino contributions for $\tilde{\mu}_1$ are shown in figure 4.11a. Note that since $M_{\tilde{e}}^{R} < M_{\tilde{e}}^{L}$, $\tilde{\mu}_1$ is mostly right-handed and $\tilde{\mu}_2$ mostly left-handed for low values of μ. At higher values for μ, the effect of mixing becomes more prevalent. The neutralino contributions for $\tilde{\mu}_2$ are shown in figure 4.11b. When we look at the individual neutralino contributions we see that $\tilde{\chi}_1^0$ is responsible for the linear behaviour after $\mu = M_2$. For the heavy smuon, this contribution is negative but smaller. This

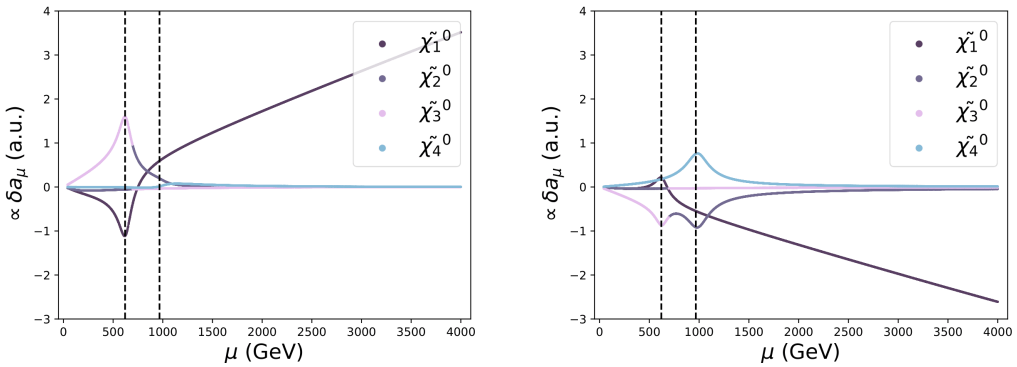

(A) The neutralino contributions due to $\tilde{\mu}_1$ when varying μ.

(B) The neutralino contributions due to $\tilde{\mu}_2$ when varying μ.

FIGURE 4.11: The neutralino contributions due to the two different smuons. The dashed lines indicate the values for which $|\mu|$ crosses $M_1 = 620$ GeV and $M_2 = 966$ GeV.

results in a positive linear dependence at higher values of μ.

The dip in the neutralino contribution at low values of μ is caused by the third neutralino (which is the Bino-like neutralino up to roughly $\mu = 620$ Gev) for the heavy smuon contribution and the first neutralino (the Higgsino-like neutralino up to roughly 620 GeV) for the light smuon. Because the first neutralino hardly contributes up to roughly 400 GeV for the heavy smuon, the significant total positive contribution comes from the third neutralino in the light smuon figure. To see why this is, we need to have a close look at the expression for the couplings n^L_{im} and n^R_{im}. We will repeat them here:

$$n^L_{im} = \frac{1}{\sqrt{2}}(g_1 N_{i1} + g_2 N_{i2}) X^*_{m1} - y_\mu N_{i3} X^*_{m2}$$
$$n^R_{im} = \sqrt{2} g_1 N_{i1} X_{m2} + y_\mu N_{i3} X_{m1}.$$

Let us focus on the product of left-and right coupling, as the squared coupling terms scale with the mass of the muon and are thus suppressed. When $\mu \approx 0$, there is no mixing between the smuon states. As $M^L_{\tilde{e}}$ is larger than $M^R_{\tilde{e}}$, the lightest smuon will be right-handed. This means we effectively have to rotate the smuon mixing matrix X, see equation 2.6. Hence, the off-diagonal terms of X are significant and the diagonal terms are zero (i.e. $X_{11} = X_{22} = 0$) at $\mu = 0$. Even when μ increases, the diagonal terms will remain small in comparison to the off-diagonal terms. Hence, if we take $m = 1$, the dominant contributing terms are:

$$n^L_{i1} n^R_{i1} = -y_\mu N_{i3} X^*_{12} \sqrt{2} g_1 N_{i1} X_{12}.$$

If we look at the third neutralino, we have $i = 3$. This means we have the matrix elements N_{33} and N_{31} contributing. N_{33} is negative and N_{31} is positive, resulting in a positive contribution for the lightest smuon. For the heavy smuon we have $m = 2$, thus the opposite terms survive in the product of couplings:

$$n^L_{i2} n^R_{i2} = \frac{1}{\sqrt{2}}(g_1 N_{i1} + g_2 N_{i2}) X^*_{21} y_\mu N_{i3} X_{21}.$$

Again, N_{33} is negative and both N_{31} and N_{32} are positive. This explains why the third neutralino $\tilde{\chi}^0_3$ has a positive contribution for the lightest smuon and a negative contribution for the heavy smuon. Finally, N_{32} is negligibly small, so $g_1 N_{i1} + g_2 N_{i2} \approx g' N_{i1}$. This explains why the overall factor between the two contributions for $\tilde{\chi}^0_3$ is approximately -2.

For the first neutralino we can use the same reasoning. The difference however, is that we now have the matrix elements N_{11}, N_{12} and N_{13} in the products. Both N_{11} and N_{13} are negative, explaining the negative contribution of $\tilde{\chi}^0_1$ for the lightest smuon and the positive contribution for the heavy smuon. The reason $\tilde{\chi}^0_1$ hardly contributes for the heavy smuon up to $\mu \approx 400$ GeV is because of the $(g_1 N_{11} + g_2 N_{12})$ term. N_{12} is positive here, but only slightly smaller than N_{11}, making $(g_1 N_{11} + g_2 N_{12})$ very small and negative.

We also see that the fourth neutralino hardly has any contribution for the mostly right-handed $\tilde{\mu}_1$. This is the Wino-like neutralino for $|\mu| < |M_2|$ and only couples to left-handed particles. We do see it contribute for $\tilde{\mu}_2$, but it decreases at higher values of μ. This decrease is due to the mixing of the left-and right-handed states.

Lastly, the swap between the contributions of $\tilde{\chi}_2^0$ and $\tilde{\chi}_3^0$ at $\mu \approx 700$ GeV can be explained by looking at the mass of the nearly purely Higgsino state as explained for the parameter variation of M_1. As one of the neutralino is nearly purely a Higgsino state and the other is mostly Higgsino with a mix of Bino and Wino, their masses will change in a different way when varying a specific parameter. At $\mu \approx 700$ GeV, the nearly pure Higgsino state becomes the heavier state and thus becomes $\tilde{\chi}_3^0$.

Other parameters
In the parameter dependence explained above, the rest of the parameters were kept constant at 4 TeV, as to minimise their influences. As they do not appear in the equations 3.1 and 3.4, these parameters should at first glance not have any influence at all. If we vary only one of these parameters and keep all other parameters constant, we do however see a parameter dependence. Depending on which parameter we vary, there can be changes in δa_μ. This is because of the RGEs as explained in chapter 2.2.

4.4 Differences between SuperISO and MicrOMEGAs

Now that we know how δa_μ changes depending on the different pMSSM parameters at first-order, we can take a closer look at the differences between MicrOMEGAS and SuperISO.

First-order difference
If we focus on only the first-order contributions that both programs calculate, we already see a difference in output. To display this, we plot the first-order contribution of SuperISO versus the contribution of MicrOMEGAs in figure 4.12. We colour coded the points according to their $\tan\beta$ value, as the programs handle the implementation of this value differently. Any point deviating from the diagonal line $y = x$

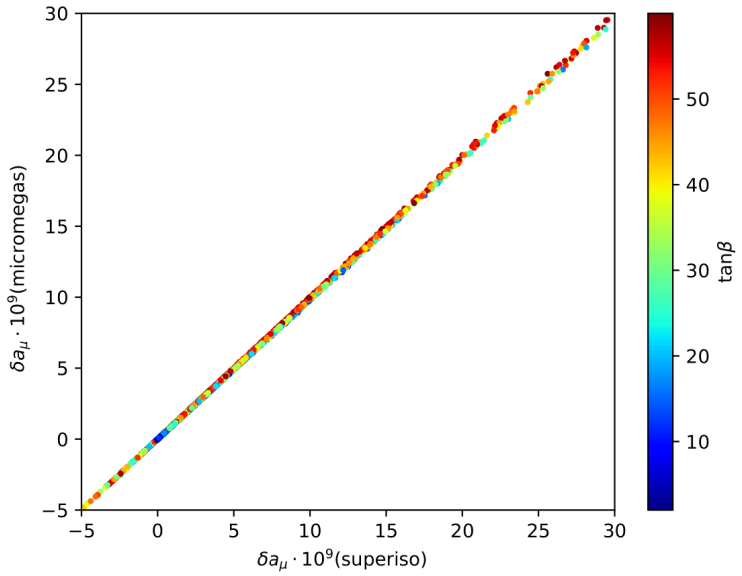

FIGURE 4.12: The first-order output for δa_μ from SuperISO vs MicrOMEGAs where the colour indicates the value of $\tan\beta$.

signifies a difference in output between the programs. The further the point is away from the diagonal, the bigger the deviation.

The difference between MicrOMEGAs and SuperISO is very subtle in figure 4.12, but it is there and is not constant. Both programs use the same equations to calculate the first-order contribution, but they do not use the same values for the variables that go into these equations. An example are constants like m_μ, whose value is more precise in one of the programs. Another difference is the scale at which the programs implement certain variables. An example of this would be $\tan\beta$. In the spectrum file given by SPheno, the input value for $\tan\beta$ is given, but also the running value of $\tan\beta$ at the scale of m_Z. These differ slightly due to the running of the parameters. In the end, multiple of these small differences lead to a difference in output.

The most important variables that differ between programs are listed in table 4.4.

Parameter	MicrOMEGAs	SuperISO
m_μ	Hardcoded at 0.1057	Hardcoded at 0.10565
m_Z	Hardcoded at 91.1876	Taken from spectrum file
m_W	Calculated by $m_Z \cos\theta_w$	Taken from spectrum file
$\sin\theta_w$	Hardcoded at $7.81653 \cdot 10^{-3}$	Calculated by $\sin\arctan g'/g$
$\tan\beta$	Taken from input file	Taken from spectrum file
g_1	Calculated by $\sqrt{4\pi\alpha_{em}}/\cos\theta_w$	Hardcoded at 0.357458
g_2	Calculated by $\sqrt{4\pi\alpha_{em}}/\sin\theta_w$	Harddcoded at 0.651908

TABLE 4.4: The largest differences in variables for the first-order calculations of MicrOMEGAs and SuperISO.

Overall, the different choices for hardcoding the variables versus taking them from the spectrum file leads to a difference between the programs of roughly $1-5\%$. Since this discrepancy is small enough to fall within the error of Δa_μ we conclude that the output of the programs at first-order is consistent.

Higher orders
When one takes into account the second-order contributions of SuperISO and the correction SuperISO applies to the first-order contribution, one generally expects a larger difference between the programs. However, for most parameter sets the second order contributions are small. If the higher-order contributions would be smaller than the difference in first-order contributions between MicrOMEGAs and SuperISO, then one can neglect the higher-order contributions entirely. This is often the case. However, from equations 3.8 and 3.9, we see that m_A and A_t are expected to have a large impact on the second-order contributions to δa_μ. Parameter sets with extreme values for these parameters could result in large second-order contributions for which it is important to take the extra contributions of SuperISO into account.

In order to quantify the contribution of second-order diagrams, we did multiple random scans with extra constraints, where all contributions calculated by SuperISO were taken into account. The scans with extra constraints include the constraint that

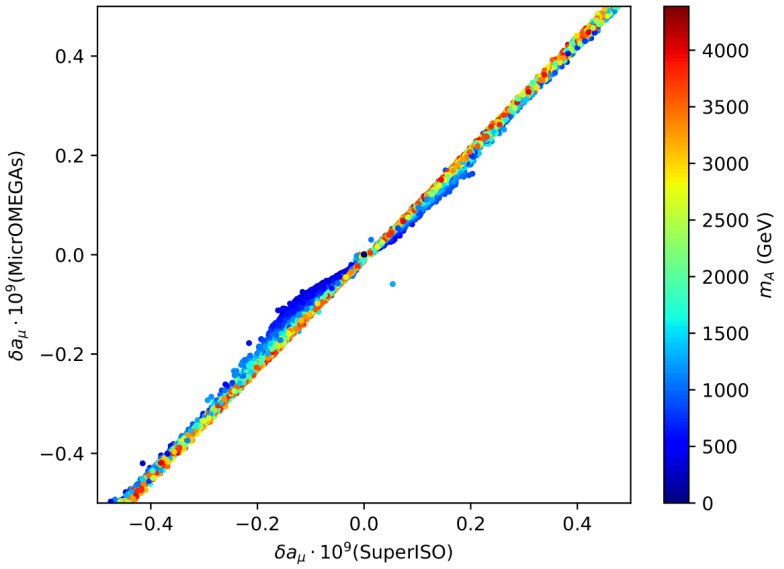

FIGURE 4.13: The output for δa_μ from SuperISO vs MicrOMEGAs where the colour indicates the value of m_A. The figure is zoomed into the region where $-0.5 \cdot 10^{-9} < \delta a_\mu < 0.5 \cdot 10^{-9}$.

one Higgs boson should have a mass of 125 ± 4 GeV and the supersymmetric particle lowest in mass should be neutral. For each of the 19 specific parameters, the output of the full SuperISO calculation for δa_μ was then plotted against the first-order contribution calculated by MicrOMEGAs and colour coded. Let us first look at m_A in figure 4.13. Note that the data set for figure 4.13 included contributions up to $\delta a_\mu \approx 2.5 \cdot 10^{-9}$, but the largest deviations from the diagonal are seen around small values for δa_μ. This is why the figure only displays a specific region of the data set.

As mentioned in chapter 3.2, we expect the second order contributions to be large when m_A is small. For regions where the second order contributions are negligible, we expect a diagonal line with a slight offset due to the first order differences. We see a small deviation from this around zero, where the absolute value of the SuperISO contribution is larger than the MicrOMEGAs one. The colour coding shows that these points are in fact all parameter sets with a small value of m_A, as was predicted to be the case. Especially the colour gradient is of interest here. As the value of m_A increases, we see the points going closer towards the diagonal.

The first-order contributions are estimated to be small when $M_{\tilde{e}}^L$ becomes large. If we would look at the same data, but colour code it for the value of $M_{\tilde{e}}^L$, we would see that almost all points that deviate from the diagonal have a high value for $M_{\tilde{e}}^L$. This means that if you allow δa_μ to be small in your parameter scans, the second order contributions will be more important relative to the first-order contributions if the first-order contributions are very small.

In figure 4.12 we showed the difference in first-order contributions for both programs, colour coded according to the value of $\tan\beta$. Figure 4.14 shows a similar picture, but now with SuperISOs second-order contributions included. Here we can

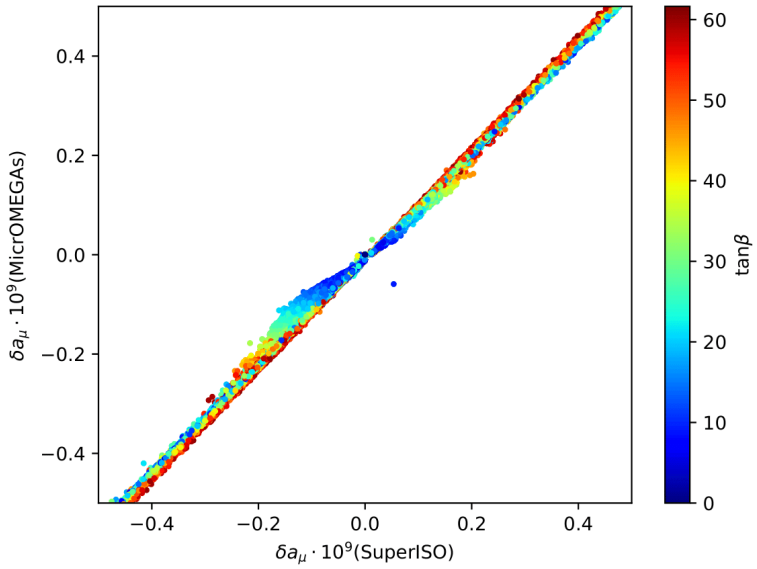

FIGURE 4.14: The output for δa_μ from SuperISO vs MicrOMEGAs where the colour indicates the value of $\tan\beta$. The figure is zoomed into the region where $-0.5 \cdot 10^{-9} < \delta a_\mu < 0.5 \cdot 10^{-9}$.

more clearly see that the deviation from the diagonal is larger when the value of $\tan\beta$ is larger.

It is hard to quantify exactly when the first-order contributions calculated by MicrOMEGAs are not precise enough due to large second-order contributions. However, we can conclude that one can better use SuperISO when allowing parameter scans to include low values of m_A and high values of $M_{\tilde{e}}^L$. We have also checked that values close to zero for μ, M_1 and M_2 lead to deviations from the diagonal. Combinations of these values for the mentioned parameters can also lead to high second-order contributions, as can specific values for $\tan\beta$, A_t, A_τ and A_b.

We have looked at how large these second order contributions can become, and thus how far the deviation from the diagonal can become. This required a parameter scan that was aimed at looking for large second-order contributions and thus no longer random. Points from this specific search were added to the data set used in the previous figures. These points are rare to find in a random scan, but can definitely exist. Figure 4.15 shows the data set but with the added points, again colour coded according to the value of m_A as this should have the largest influence on second-order contributions.

The scale of the axis has been increased in figure 4.15 such that the extreme deviations from the diagonal are more visible. The extra points on the right of the diagonal are the points added artificially to the data set to show how large these deviations can become. The right-most point is one that borders the limitations of what is still allowed due to the constraints, i.e. it does not lead to a tachyonic particle.

We also see from the figure that at higher values of δa_μ the deviation from the diagonal increases overall. Note that these points at higher values for δa_μ were present

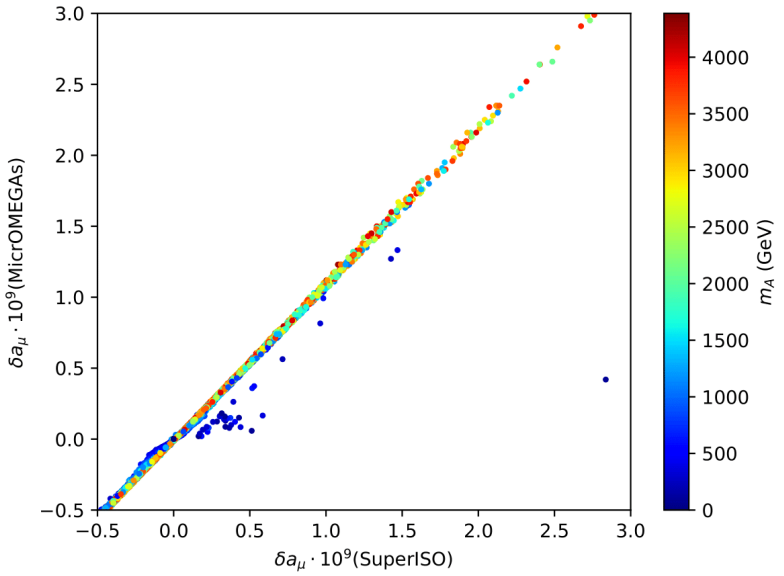

FIGURE 4.15: The output for δa_μ from SuperISO vs MicrOMEGAs where the colour indicates the value of $\tan\beta$. The figure is zoomed into the region where $-0.5 \cdot 10^{-9} < \delta a_\mu < 3.0 \cdot 10^{-9}$.

in the original data set and have not been artificially added here. The reason for MicrOMEGAs giving a higher value than SuperISO for most of these points is because of the extra factor with which SuperISO corrects the first-order contributions, given by equation 3.6. This factor always causes a reduction in the first-order contribution and thus has a significant effect especially when the Barr-Zee contributions are negligible. For high values of δa_μ, this factor could increase the difference between the output of SuperISO and MicrOMEGAs to be significant with respect to the error on Δa_μ.

If one is interested in using MicrOMEGAs or SuperISO to solve the anomalous magnetic moment problem in the SM, one would be searching for specific parameter sets that give a value for δa_μ of roughly $2.68 \cdot 10^{-9}$. If one samples the pMSSM space randomly with a constraint built in where $\delta a_\mu = 2.68 \cdot 10^{-9} \pm 0.9 \cdot 10^{-9}$, it is very likely that the first-order contribution is enough. As soon as one allows more extreme values for the parameters though, one can quickly stumble upon parameter sets for which the second-order contributions matter. We therefore recommend using SuperISO over MicrOMEGAs for the purpose of δa_μ calculations, as we cannot give a clear condition for when first-order calculations of MicrOMEGAs are always sufficient.

Conclusion

In this thesis we have shown how the theoretical calculation for the anomalous magnetic moment of the muon is structured. We have shown the extra contributions that arise if one extends the SM with the pMSSM and we have argued that all 19 input parameters of the pMSSM can have an effect on δa_μ, but that only certain parameters have the most direct influence.

We focused on two specific programs used by many in the SUSY theory community: MicrOMEGAs and SuperISO. The biggest difference between the output of MicrOMEGAs and SuperISO comes from the fact that the programs calculate the contributions up to different orders. Both programs calculate the full first-order contribution, which agree up to sufficient precision. Only SuperISO implements a general correction factor that arises from similar diagrams but with higher-order loops in them. Besides that, SuperISO also incorporates a new type of diagram that only appears at second-order or higher, called Barr-Zee diagrams. SuperISO calculates the largest contributions coming from these Barr-Zee diagrams and adds these to the corrected first-order contribution.

When performing random scans in the pMSSM parameter space, one will often find small contributions from these second-order diagrams that SuperISO calculates. However, we have shown that it is possible to find points in the pMSSM parameter space for which the second-order Barr-Zee contributions can become large. In this region of parameter space, MicrOMEGAs would not give sufficiently precise results.

When the second-order contributions are small, the correction factor applied to the first-order contributions causes the largest difference between the programs. This results in MicrOMEGAs often giving a higher output than SuperISO, as the correction is always negative. The only way SuperISO can have a higher output would be if the second-order Barr-Zee contributions are large enough to overcome the first-order correction factor or if δa_μ is negative.

Because of the above mentioned reasons, we suggest using SuperISO for calculations to the anomalous magnetic moment of the muon. Even though MicrOMEGAs will often give a similar result, within the SM error, to that of SuperISO, there are parameter sets for which the differences become large. We cannot give clear limitations on the parameters for which MicrOMEGAs will give a similar result to SuperISO, so it is safest to always use SuperISO.

If the newest experiment improves the experimental error but keeps the experimental value the same, the deviation between experiment and the SM theoretical value becomes significant enough to warrant a new physics explanation. We have shown that the pMSSM has potential to solve this deviation.

Appendix A

The second order loop functions used in the calculation by SuperISO are given by [45]:

$$\begin{aligned} F_{A^0}(x) &= x\int_0^1 \mathrm{d}z \frac{1}{z(1-z)-x}\ln\frac{z(1-z)}{x} \\ &= \frac{2x}{y}\Big[\mathrm{Li}_2\Big(1-\frac{1-y}{2x}\Big)-\mathrm{Li}_2\Big(1-\frac{1+y}{2x}\Big)\Big], \\ F_l(x) &= (2x-1)F_{A^0}(x)-2x(2+\log x), \\ F_f &= \frac{x}{2}\big(2+\log x - F_{A^0}(x)\big), \end{aligned}$$

where $y=\sqrt{1-4x}$. The Li_2 functions are Spence functions defined by:

$$\mathrm{Li}_2(z) = -\int_0^z \mathrm{d}u \frac{\ln 1-u}{u},\ \ z\in\mathbb{C}.$$

For $x > 0.25$, y becomes complex. In that case, SuperISO approximates the F_{A^0} function as:

$$\begin{aligned} x<2.5: &-0.1365013496-1.858455623\log(1+x) \\ &-0.5996763746(\log(1+x))^2+0.4390843985\sqrt{x}\log(1+x) \\ &-0.1444359743x\log(1+x)+3.852425143\sqrt{x} \\ 2.5\le x<100: &\ 0.4304425955+0.06766323794\log(1+x) \\ &-0.1584446296(\log(1.+x))^2-0.2787080541\sqrt{x}\log(1+x) \\ &+1.557845370\cdot10^{-3}x\log(1+x)+2.139180566\sqrt{(}x) \\ 100\le x<10000: &\ 2.025445594+0.9960866255\log x+1.122896720\cdot10^{-4}\sqrt{x}. \end{aligned} \tag{b.1}$$

The SPheno loop functions are given in integral representation by [49]:

$$\begin{aligned} I_1(\alpha,\beta) &= \int_0^1 \mathrm{d}x\int_0^{1-x}\mathrm{d}z\frac{-z}{\alpha z^2+(1-\alpha-\beta)z+\beta}, \\ I_2(\alpha,\beta) &= \int_0^1 \mathrm{d}x\int_0^{1-x}\mathrm{d}z\frac{z^2-z}{\alpha z^2+(1-\alpha-\beta)z+\beta}, \\ I_3(\alpha,\beta) &= \int_0^1 \mathrm{d}x\int_0^{1-x}\mathrm{d}z\frac{1-z}{\alpha z^2+(\beta-\alpha-1)z+1}, \\ I_4(\alpha,\beta) &= \int_0^1 \mathrm{d}x\int_0^{1-x}\mathrm{d}z\frac{z^2-z}{\alpha z^2+(\beta-\alpha-1)z+1}. \end{aligned}$$

When approximating $\alpha = 0$, the loop functions as used in 4.1 are found:

$$F_1(y) = 2I_1(0,y) = \frac{1}{(y-1)^3}\Big(1 - y^2 + 2y\ln(y)\Big),$$
$$F_2(y) = 6I_2(0,y) = \frac{1}{(y-1)^4}\Big(-y^3 + 6y^2 - 3y - 2 - 6y\ln(y)\Big),$$
$$F_3(y) = -2I_3(0,y) = \frac{1}{(y-1)^3}\Big(3y^2 - 4y + 1 - 2y^2\ln(y)\Big),$$
$$F_4(y) = -6I_4(0,y) = \frac{1}{(y-1)^4}\Big(2y^3 + 3y^2 - 6y + 1 - 6y^2\ln(y)\Big).$$

The argument of these loop functions is the inverse of the argument used in the SuperISO and MicrOMEGAs loop functions. Let $x = 1/y$:

$$F_1(x) = \frac{x}{(1-x)^3}\Big(-1 + x^2 - 2x\ln(x)\Big) = -\frac{1}{3}xF_2^N(x),$$
$$F_2(x) = \frac{x}{(1-x)^4}\Big(-1 + 6x - 3x^2 - 2x^3 + 6x^2\ln(x)\Big) = -\frac{1}{2}xF_1^N(x),$$
$$F_3(x) = \frac{x}{(1-x)^3}\Big(3 - 4x + x^2 + 2\log(x)\Big) = -\frac{2}{3}xF_2^C(x),$$
$$F_4(x) = \frac{x}{(1-x)^4}\Big(2 + 3x - 6x^2 + x^3 + 6x\ln(x)\Big) = \frac{1}{2}xF_1^C(x),$$

where $F_{1,2}^{N,C}$ are the loop functions used by SuperISO and MicrOMEGAs as given in chapter 3.1.

Splitting up the couplings in equations 3.1 and 3.4, reordering the constants and detaching the loop functions leads to:

$$\delta a_\mu^{\tilde{\chi}^0}(1) = \sum_{i=1}^{4}\sum_{m=1}^{2} -\frac{m_\mu}{16\pi^2}\frac{m_\mu}{12m_{\tilde{\mu}_m}^2}(\mid n_{im}^L\mid^2 + \mid n_{im}^R\mid^2)$$
$$\delta a_\mu^{\tilde{\chi}^0}(2) = \sum_{i=1}^{4}\sum_{m=1}^{2} \frac{m_\mu}{16\pi^2}\frac{1}{3}\frac{m_{\tilde{\chi}_i^0}}{m_{\tilde{\mu}_m}^2}Re[n_{im}^L n_{im}^R]$$
$$\delta a_\mu^{\tilde{\chi}^\pm}(1) = \sum_{k=1}^{2} \frac{m_\mu}{16\pi^2}\frac{m_\mu}{12m_{\tilde{\nu}_\mu}^2}(\mid c_k^L\mid^2 + \mid c_k^R\mid^2)$$
$$\delta a_\mu^{\tilde{\chi}^\pm}(2) = \sum_{k=1}^{2} \frac{m_\mu}{16\pi^2}\frac{2}{3}\frac{m_{\tilde{\chi}_k^\pm}}{m_{\tilde{\nu}_\mu}^2}Re[c_k^L c_k^R]$$

Expanding the couplings, including g_1, g_2 and y_μ leads to:

$$\begin{aligned}
\delta a_\mu^{\tilde{\chi}^0}(1) = &-\frac{m_\mu^2 \alpha_{em}}{48\pi \sin^2(\theta_w)} \sum_{i=1}^{4} \sum_{m=1}^{2} \frac{1}{m_{\tilde{\mu}_m}^2} \Big\{ \frac{m_\mu^2}{2M_W^2 \cos^2(\beta)} |N_{i3}|^2 \\
&+ \frac{1}{2} \tan^2(\theta_w) |N_{i1}|^2 (|X_{m1}|^2 + 4|X_{m2}|^2) + \frac{1}{2} |N_{i2}|^2 |X_{m1}|^2 \\
&+ \tan(\theta_w) |X_{m1}|^2 Re(N_{i1} N_{i2}^*) + \frac{m_\mu \tan(\theta_w)}{m_W \cos(\beta)} Re(N_{i3} N_{i1}^* X_{m1} X_{m2}^*) \\
&- \frac{m_\mu}{m_W \cos(\beta)} Re(N_{i3} N_{i2}^* X_{m1} X_{m2}^*) \Big\} \\
= &\frac{m_\mu^2 \alpha_{em}}{24\pi \sin^2(\theta_w)} \sum_{j=1}^{4} \sum_{k=1}^{2} \frac{1}{m_{\tilde{\chi}_j^0}^2} X_{\mu j}^k \cdot \Big[-\frac{1}{2} \frac{m_{\tilde{\chi}_j^0}^2}{m_{\tilde{\mu}_k}^2} \Big],
\end{aligned}$$

$$\begin{aligned}
\delta a_\mu^{\tilde{\chi}^0}(2) = &\frac{m_\mu \alpha_{em}}{12\pi \sin^2(\theta_w)} \sum_{i=1}^{4} \sum_{m=1}^{2} \frac{m_{\tilde{\chi}_i^0}}{m_{\tilde{\mu}_m}^2} \Big\{ \tan^2(\theta_w) Re(N_{i1}^2 X_{m1}^* X_{m2}) \\
&+ \tan(\theta_w) Re(N_{i2} N_{i1} X_{m1}^* X_{m2}) - \frac{m_\mu \tan(\theta_w)}{m_W \cos(\beta)} |X_{m2}|^2 Re(N_{i3} N_{i1}) \\
&+ \frac{m_\mu \tan(\theta_w)}{2m_W \cos(\beta)} |X_{m1}|^2 Re(N_{i3} N_{i1}) + \frac{m_\mu}{2m_W \cos(\beta)} |X_{m1}|^2 Re(N_{i3} N_{i2}) \\
&- \frac{m_\mu^2}{2M_W^2 \cos^2(\beta)} Re(N_{i3}^2 X_{m2}^* X_{m1}) \Big\} \\
= &\frac{m_\mu \alpha_{em}}{4\pi \sin^2(\theta_w)} \sum_{j=1}^{4} \sum_{k=1}^{2} \frac{1}{m_{\tilde{\chi}_j^0}} \eta_{\mu j}^k \cdot \Big[-\frac{1}{3} \frac{m_{\tilde{\chi}_j^0}^2}{m_{\tilde{\mu}_k}^2} \Big],
\end{aligned}$$

$$\delta a_\mu^{\tilde{\chi}^\pm}(1) = \frac{m_\mu^2 \alpha_{em}}{24\pi \sin^2(\theta_w)} \sum_{k=1}^{2} \frac{1}{m_{\tilde{\chi}_k^\pm}^2} \Big\{ \frac{m_\mu^2}{2M_W^2 \cos^2(\beta)} |U_{k2}|^2 + |V_{k1}|^2 \Big\} \cdot \Big[\frac{1}{2} \frac{m_{\tilde{\chi}_k^\pm}^2}{m_{\tilde{\nu}_\mu}^2} \Big],$$

$$\delta a_\mu^{\tilde{\chi}^\pm}(2) = \frac{m_\mu \alpha_{em}}{4\pi \sin^2(\theta_w)} \frac{m_\mu}{\sqrt{2} m_W \cos(\beta)} \sum_{k=1}^{2} \frac{1}{m_{\tilde{\chi}_k^\pm}} Re(U_{k2}^* V_{k1}^*) \cdot \Big[-\frac{2}{3} \frac{m_{\tilde{\chi}_k^\pm}^2}{m_{\tilde{\nu}_\mu}^2} \Big],$$

where in the last equality for each δa_μ a relabeling of the sum index was applied. The $X_{\mu j}^k$ and $\eta_{\mu j}^k$ are exactly the same as given in equations (31) and (32) of [50] and are found in equation 4.1. The terms in brackets are cancelled by the change in the argument of the loop functions as can be seen on the previous page. This proves that the seemingly different expressions in equations 3.1 and 3.4 and in the equation 4.1 are in fact almost identical. The only difference is a missing factor of 2 in the $\delta a_\mu^{\tilde{\chi}^\pm}(2)$ compared to the expressions SuperISO and MicrOMEGAs use. This difference is also present in other literature, i.e. in comparing the loop functions between [37] and [40].

Appendix B

Here we will show the characteristics of the loop functions as a function of the mass ratio x. We present a logarithmic plot of each loop function as to better understand both extremes of the mass ratio. For the F_{A^0} loop function, SuperISO uses an approximation (see appendix A). We show this approximation in figure C.7 and the correct analytical function with a better approximation in a non-logarithmic plot in figure C.8, where we zoomed in on the exact point where deviations occur.

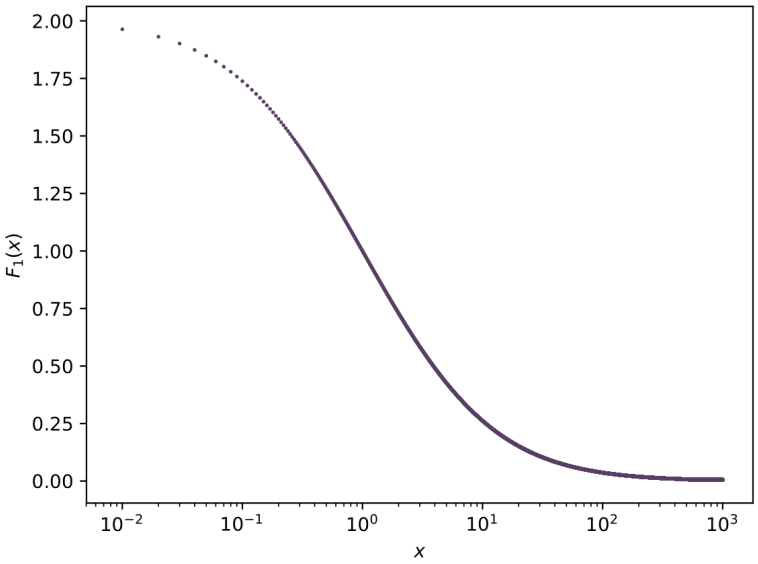

FIGURE C.1: A plot of $F_1(x) = F_1^N(x) = \frac{2}{(1-x)^4}\Big(1 - 6x + 3x^2 + 2x^3 - 6x^2 \ln(x)\Big)$ on a logarithmic scale.

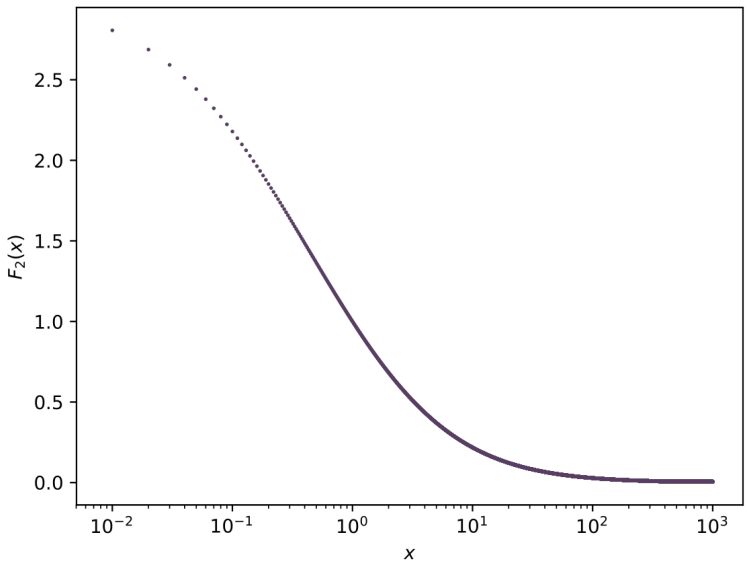

FIGURE C.2: A plot of $F_2(x) = F_2^N(x) = \frac{3}{(1-x)^3}\Big(1 - x^2 + 2x\ln(x)\Big)$ on a logarithmic scale.

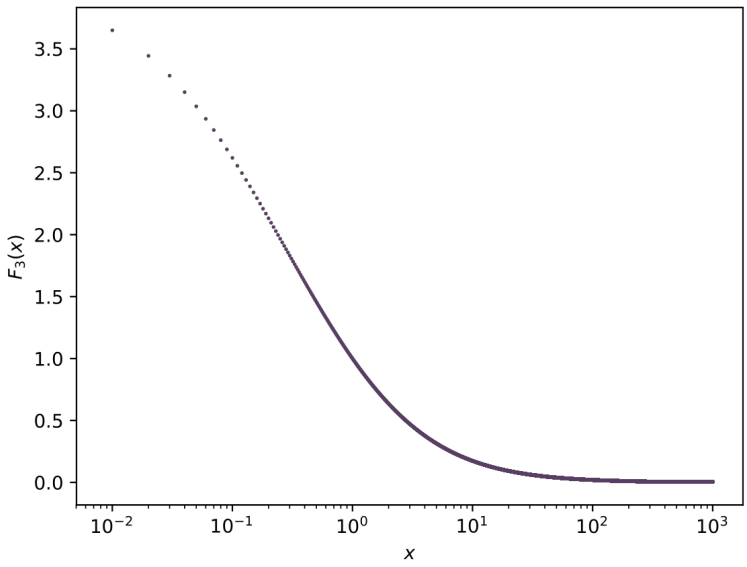

FIGURE C.3: A plot of $F_3(x) = F_1^C(x) = \frac{2}{(1-x)^4}\Big(2 + 3x - 6x^2 + x^3 + 6x\ln(x)\Big)$ on a logarithmic scale.

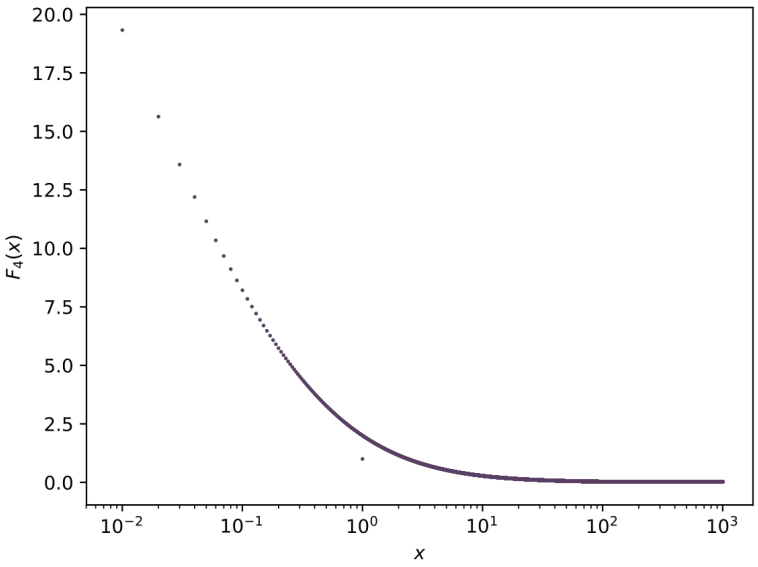

FIGURE C.4: A plot of $F_4(x) = F_2^C(x) = \frac{3}{2(1-x)^3}\Big(-3 + 4x - x^2 - 2\log(x)\Big)$ on a logarithmic scale

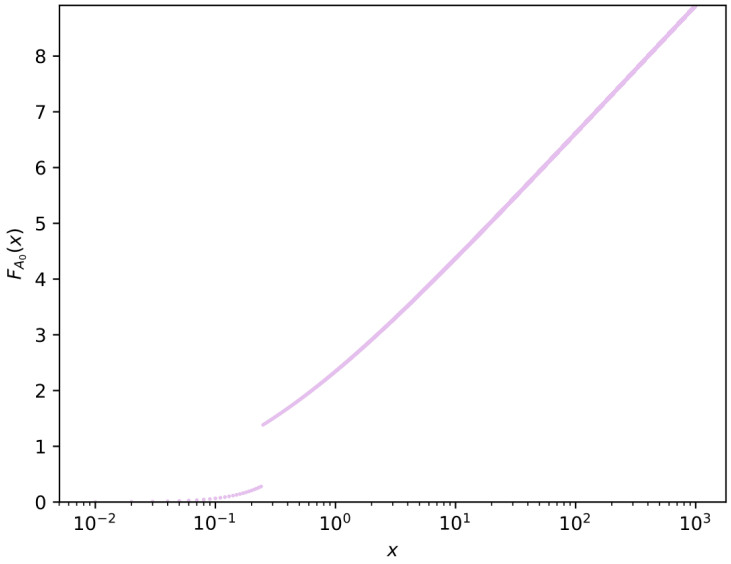

FIGURE C.5: A plot of $F_{A^0}(x) = x\int_0^1 \mathrm{d}z \frac{1}{z(1-z)-x} \ln\frac{z(1-z)}{x}$ on a logarithmic scale as approximated by SuperISO.

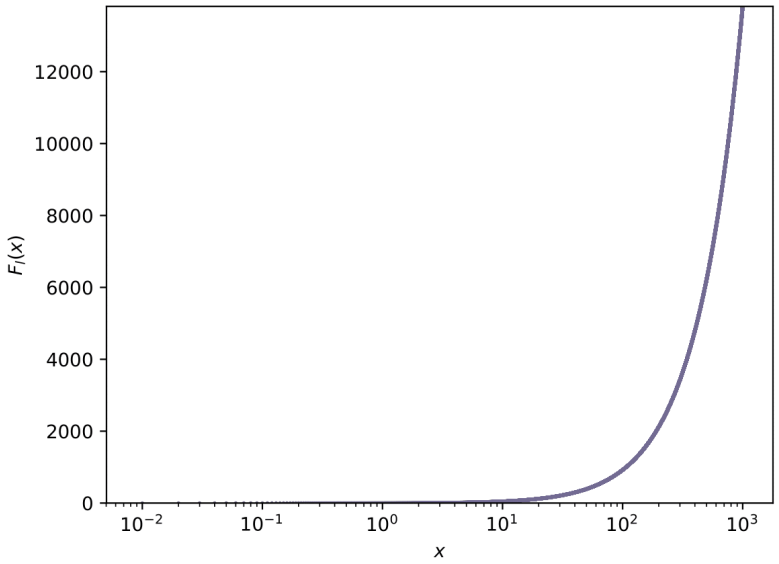

FIGURE C.6: A plot of $F_l(x) = (2x-1)F_{A^0}(x) - 2x(2+\log x)$ on a logarithmic scale.

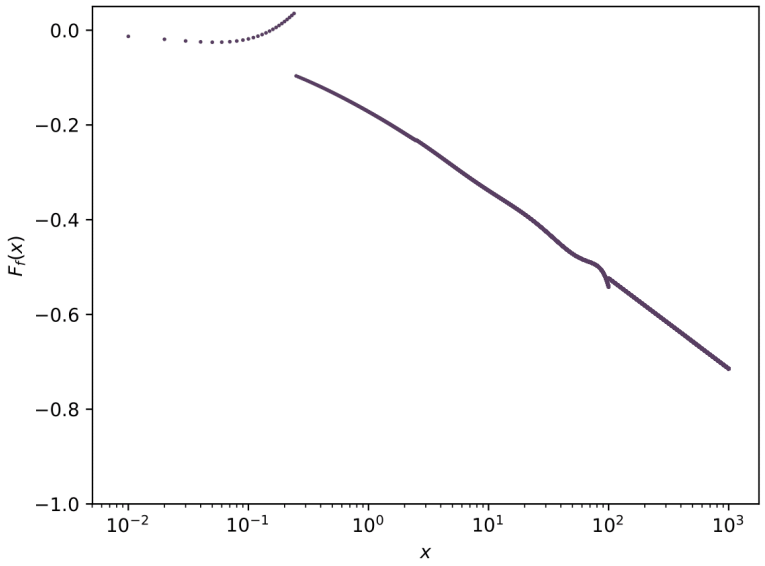

FIGURE C.7: A plot of F_f as approximated by SuperISO on a logarithmic scale.

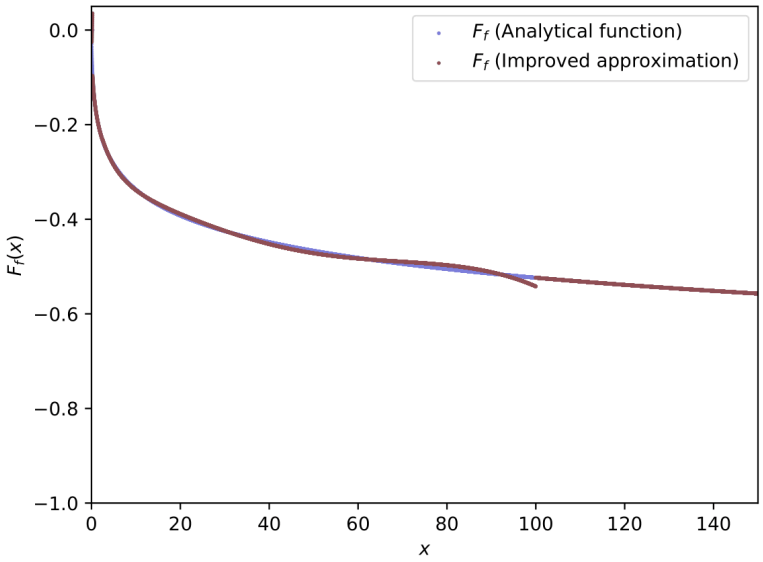

FIGURE C.8: A plot of the analytical function of $F_f = \frac{x}{2}\big(2 + \log x - F_{A^0}(x)\big)$ from $x = 0$ to $x = 150$ to show the deviation between the analytical function and the approximation made by SuperISO.

Bibliography

[1] M. Passera G. F. Giudicea P. Paradisi. "Testing new physics with the electron $g-2$". In: *CERN-PH-TH/2012-017* (2012). URL: https://arxiv.org/pdf/1208.6583.pdf.

[2] G.W. Bennett et al. "Final report of the E821 muon anomalous magnetic moment measurement at BNL". In: *Physical Review* D 73 (2006). URL: https://journals.aps.org/prd/pdf/10.1103/PhysRevD.73.072003.

[3] W.J. Marciano A. Hoecker. "57. Muon Anomalous Magnetic Moment". In: *Particle Data Group* (2019). URL: https://pdg.lbl.gov/2019/reviews/rpp2018-rev-g-2-muon-anom-mag-moment.pdf.

[4] M. Passera S. Eidelman. "Theory of the τ lepton anomalous magnetic moment". In: D 73 (2007). URL: https://arxiv.org/pdf/hep-ph/0701260.pdf.

[5] J.D. Jackson. "chapter 5. Magnetostatics". In: *Classical Electrodynamics* (1962), pp. 132–162.

[6] O. Certík. "8.3. Quantum Electrodynamics (QED)". In: (2009). URL: https://www.theoretical-physics.net/dev/quantum/qed.html.

[7] J.D. Björken and S.D. Drell. "Chapter 4: The Foldy-Wouthuysen Transformation". In: *Relativistic Quantum Mechanics* (1964), pp. 46–52.

[8] F. Jegerlehner. "Chapter 3.1: Equation of Motion for a Lepton in an External Field". In: *The Anomalous Magnetic Moment of the Muon* 2nd edition (2017), pp. 163–168.

[9] P.A.M. Dirac. "The Quantum Theory of the Electron". In: *Proceedings of the Royal Society* 117 (1928). URL: http://wwwhome.lorentz.leidenuniv.nl/~boyarsky/media/Proc.R.Soc.Lond.-1928-Dirac-610-24.pdf.

[10] L.H. Thomas B.A. "I. The kinematics of an electron with an axis". In: *The London, Edinburgh, and Dublin Philosophical Magazine and Journal of Science* 3:13 (1927), pp. 1–22. URL: http://dx.doi.org/10.1080/14786440108564170.

[11] Y.M. Galperin. "Dynamics of Bloch Electrons". In: *Introduction to Modern Solid State Physics* (2014), pp. 57–63.

[12] L. Michel V. Bargmann and V.L. Telegdi. "Precession of the Polarization of Particles moving in a Homogeneous Electromagnetic Field". In: *Physical Review* Letter 2 (1959). URL: https://journals.aps.org/prl/pdf/10.1103/PhysRevLett.2.435.

[13] J. Mot. "The Muon $g-2$ experiment at Fermilab". In: *Hyperfine Interactions* 239.55 (2018). URL: https://lss.fnal.gov/archive/2017/conf/fermilab-conf-17-216-e.pdf.

[14] Y. Nagashima. "Elementary Particle Physics". In: Volume 2: Foundations of the Standard Model, Appendix B (2013), pp. 507–509.

[15] M.E. Peskin and D.V. Schroeder. "An Introduction to Quantum Field Theory". In: 1st edition (1995), pp. 185–187.

[16] F. Jegerlehner. "Chapter 3: Lepton Magnetic Moments: Basics". In: *The Anomalous Magnetic Moment of the Muon* 2nd edition (2017), pp. 202–210.

[17] J. Gluza and T. Riemann. "Lecture: Evaluation of Feynman Integrals: Advanced Methods". In: Allahabad, India (2009), pp. 13–14. URL: https://www-zeuthen.desy.de/~riemann/Talks/riemann-recapp-09.pdf.

[18] M.E. Peskin and D.V. Schroeder. "An Introduction to Quantum Field Theory". In: 1st edition (1995), pp. 192–193.

[19] B. Krause A. Czarnecki. "Electroweak corrections to the muon anomalous magnetic moment". In: *Nuclear Physics B* 51 C (1996), pp. 148–153. URL: https://arxiv.org/abs/hep-ph/9606393.

[20] D. Stöckinger S. Heinemeyer and G. Weiglein. "Electroweak and supersymmetric two-loop corrections to $(g-2)_\mu$". In: *Nuclear Physics* B 699 (2004), pp. 103–123. URL: https://arxiv.org/pdf/hep-ph/0405255.pdf.

[21] T. Kinoshita and M. Nio. "Tenth-order QED contribution to the lepton $g-2$: Evaluation of dominant α^5 terms of muon $g-2$". In: *Physical Review* D 73.053007 (2006). URL: https://journals.aps.org/prd/pdf/10.1103/PhysRevD.73.053007.

[22] A.D. Martin D. Nomura K. Hagiwara A. Keshavarzi and T. Teubner. "g-2 of the muon: status report". In: *Nuclear and Particle Physics Proceedings* 278-288 (2017), pp. 33–38. URL: https://doi.org/10.1016/j.nuclphysbps.2017.03.039.

[23] I.Bars and M.Yoshimura. "Muon Magnetic Moment in a Finite Theory of Weak and Electromagnetic Interactions". In: *Physical Review* 6.1 (1972), pp. 103–123. URL: https://journals.aps.org/prd/pdf/10.1103/PhysRevD.6.374.

[24] A.Schiller T.V.Kukhto E.A.Kuraev and Z.K.Silagadze. "The dominant two-loop electroweak contributions to the anomalous magnetic moment of the muon". In: *Nuclear Physics B* 371 (1972), pp. 567–596. URL: https://doi.org/10.1016/0550-3213(92)90687-7.

[25] W.J. Marciano A. Czarnecki B. Krause. "Electroweak Fermion-loop Contributions to the Muon Anomalous Magnetic Moment". In: *Physical Review* D 52 (1995), pp. 2619–2623. URL: https://arxiv.org/pdf/hep-ph/9506256.pdf.

[26] H. Joos M. Böhm A. Denner. "Gauge Theories of the Strong and Electroweak Interaction". In: (), pp. 671–704. URL: https://doi.org/10.1007/978-3-322-80160-9.

[27] B. Malaescu M. Davier A. Hoecker and Z. Zhang. "Reevaluation of the hadronic vacuum polarisation contributions to the Standard Model predictions of the muon g-2 and alpha(mZ) using newest hadronic cross-section data". In: *European Physical Journal* C 77 (2017), pp. 567–596. URL: https://arxiv.org/abs/1706.09436.

[28] M.Gourdin and E.De Rafael. "Hadronic contributions to the muon g-factor". In: *Nuclear Physics B* 10.4 (1969), pp. 667–674. URL: https://doi.org/10.1016/0550-3213(69)90333-2.

[29] E. de Rafael J. Prades and A. Vainshtein. "Hadronic Light-by-Light Scattering Contribution to the Muon Anomalous Magnetic Moment". In: (2017). URL: https://arxiv.org/abs/0901.0306.

[30] H. Murayama. "Supersymmetry Phenomenology". In: 18 (2000). URL: https://arxiv.org/pdf/hep-ph/0002232.pdf.

[31] S.P. Martin. "A Supersymmetry Primer (v7)". In: *Adv. Ser. Direct. High Energy Phys* 18.1 (2016), pp. 3–12. URL: https://arxiv.org/abs/hep-ph/9709356.

[32] S.P. Martin. "A Supersymmetry Primer (v7)". In: *Adv. Ser. Direct. High Energy Phys* 18.1 (2016), pp. 72–95. URL: https://arxiv.org/abs/hep-ph/9709356.

[33] A. Vainshtein K. Melnikov. "Theory of the Muon Anomalous Magnetic Moment". In: (2006), pp. 152–154.

[34] S.P. Martin. "A Supersymmetry Primer (v7)". In: *Adv. Ser. Direct. High Energy Phys* 18.1 (2016), pp. 66–72. URL: https://arxiv.org/abs/hep-ph/9709356.

[35] S.P. Martin. "A Supersymmetry Primer (v7)". In: *Adv. Ser. Direct. High Energy Phys* 18.1 (2016), pp. 85–114. URL: https://arxiv.org/abs/hep-ph/9709356.

[36] J. Rosiek. "Complete set of Feynman rules for the MSSM – ERRATUM". In: Appendix B (2002). URL: https://arxiv.org/abs/hep-ph/9511250.

[37] J.D. Wells S.P. Martin. "Muon anomalous magnetic dipole moment in supersymmetric theories". In: *Physical Review* D64 (2001), p. 035003. URL: https://arxiv.org/abs/hep-ph/0103067.

[38] G.F. Giudice G. Degrassi. "QED Logarithms in the Electroweak Corrections to the Muon Anomalous Magnetic Moment". In: *Physical Review* D58 (1998), p. 053007. URL: https://arxiv.org/abs/hep-ph/9803384.

[39] C.H. Chou W.Y. Keung D. Chang W.F. Chang. "Large Two-Loop Contributions to g-2 from a Generic Pseudoscalar Boson". In: *Physical Review* D63 (2001), p. 091301. URL: https://arxiv.org/abs/hep-ph/0009292.

[40] D. Stöckinger. "The Muon Magnetic Moment and Supersymmetry". In: *Journal of Physics* G34 (2006). URL: https://arxiv.org/pdf/hep-ph/0609168.pdf.

[41] X.F. Han L. Wang. "A light pseudoscalar of 2HDM confronted with muon g-2 and experimental constraints". In: *Journal of High Energy Physics* 39 (2015). URL: https://arxiv.org/pdf/1412.4874.pdf.

[42] A. Czarnecki T. Gribouk. "Electroweak interactions and the muon $g-2$: bosonic two-loop effects". In: *Physical Review* D72 (2005), p. 053016. URL: https://arxiv.org/abs/hep-ph/0509205.

[43] L. Lin J. Maalampi H.S. Song T.F. Feng X.Q. Li. "The two-loop supersymmetric corrections to lepton anomalous magnetic and electric dipole moments". In: *Physical Review* D73 (2006), p. 116001. URL: https://arxiv.org/abs/hep-ph/0604171.

[44] G. Weiglein S. Heinemeyer D. Stöckinger. "Two-Loop SUSY Corrections to the Anomalous Magnetic Moment of the Muon". In: *Nuclear Physics* B690 (2004), pp. 62–80. URL: https://arxiv.org/abs/hep-ph/0312264.

[45] F. Mahmoudi. "SuperIso v3.0: A program for calculating flavor physics observables in 2HDM and supersymmetry". In: *Computer Physics Communications* 180 (2009), pp. 1579–1613. URL: http://superiso.in2p3.fr/superiso3.4.pdf.

[46] A. Goudelis A. Pukhov B. Zaldivár G. Bélanger F. Boudjema. "micrOMEGAs5.0 : freeze-in". In: *Computer Physics Communications* 231 (2018), pp. 275–315. URL: https://arxiv.org/pdf/1801.03509.pdf.

[47] W. Porod. "SPheno, a program for calculating supersymmetric spectra, SUSY particle decays and SUSY particle production at e+ e- colliders". In: *Computer Physics Communications* 153 (2003), pp. 275–315. URL: http://de.arxiv.org/abs/hep-ph/0301101v4.

[48] P. Skands et al. "SUSY Les Houches Accord: Interfacing SUSY Spectrum Calculators, Decay Packages, and Event Generators". In: *Journal of High Energy Physics* 0407:036 (2004). URL: https://arxiv.org/abs/hep-ph/0311123v4.

[49] T. Ibrahim and P. Nath. "Effects of large CP violating phases on $g_\mu 2$ in MSSM". In: *Physical Review* D62.015004 (2000). URL: https://arxiv.org/pdf/hep-ph/9908443.pdf.

[50] T. Ibrahim and P. Nath. "CP violation and the muon anomaly in $N = 1$ supergravity". In: *Physical Review* D61.95008 (2000). URL: https://journals.aps.org/prd/pdf/10.1103/PhysRevD.61.095008.